ORNL-3887
UC-34 – Physics

DIFFERENTIAL CROSS SECTIONS FOR THE PRODUCTION OF PROTONS IN THE REACTIONS OF 160-MeV PROTONS ON COMPLEX NUCLEI

R. W. Peelle
T. A. Love
N. W. Hill
R. T. Santoro

OAK RIDGE NATIONAL LABORATORY
operated by
UNION CARBIDE CORPORATION
for the
U.S. ATOMIC ENERGY COMMISSION

Printed in USA. Price $4.00 . Available from the Clearinghouse for Federal
Scientific and Technical Information, National Bureau of Standards,
U.S. Department of Commerce, Springfield, Virginia 22151

LEGAL NOTICE

ORNL-3887

Contract No. W-7405-eng-26

Neutron Physics Division

DIFFERENTIAL CROSS SECTIONS FOR THE PRODUCTION OF PROTONS IN THE REACTIONS OF 160-MeV PROTONS ON COMPLEX NUCLEI

R. W. Peelle, T. A. Love, N. W. Hill,*
and R. T. Santoro

NOTE:

This Work Partially Supported by
NATIONAL AERONAUTICS AND SPACE ADMINISTRATION
Under Order R-104(1)

*Instrumentation and Controls Division.

SEPTEMBER 1966

OAK RIDGE NATIONAL LABORATORY
Oak Ridge, Tennessee
operated by
UNION CARBIDE CORPORATION
for the
U.S. ATOMIC ENERGY COMMISSION

CONTENTS

DIFFERENTIAL CROSS SECTIONS FOR THE PRODUCTION OF PROTONS IN THE REACTIONS OF 160-MEV PROTONS ON COMPLEX NUCLEI*

R. W. Peelle, T. A. Love, N. W. Hill, and R. T. Santoro

ABSTRACT

Differential cross sections in angle and energy were obtained by flight-time spectrometry for secondary protons above 20 MeV from 160-MeV protons on Be, C, H_2O, Aℓ, Co, and Bi targets. Enough angles were studied for rough angular distributions to be presented for aluminum and cobalt. All secondary charged particles were assumed to be protons, for which the energy resolution varied from 25 to 50%. The observed differential cross sections change smoothly with angle and target mass, and show no peak corresponding to quasi-free scattering near the energy corresponding to free nucleon-nucleon scattering. The measurements are compared with others available at the same energy and with intranuclear cascade estimates, including evaporation. The observed cross sections are larger than the estimated ones at angles of 90 and 120°, and at low energies for angles more forward than 45°. At 60° the observed cross sections are in accord with the Monte Carlo estimates.

+ UTHOR

I. INTRODUCTION

This report presents the methods and results of an experiment conducted at the Harvard Synchrocyclotron to determine a series of differential cross sections for the production of secondary protons in the interactions of 160-MeV protons on complex nuclei (C, O, Be, Aℓ, Co, Bi). Data on production of neutron secondaries were obtained during the same series of experiments; in fact, the results given here are from a derivative experiment which utilized much equipment designed for fast-neutron spectrometry. This link explains the unnatural use here of flight-time spectrometry.

We initiated the experiment in order to increase our knowledge of the production of secondary nucleons by protons in the energy region significant for manned spaceflight.[1] While charged reaction products

*Work funded by the National Aeronautics and Space Administration under NASA Order R-104(1).

[1]F. C. Maienschein, Neutron Phys. Div. Space Rad. Shielding Res. Ann. Progr. Rept. Aug. 31, 1962, ORNL CF-62-10-29, pp. 172-181.

themselves constitute a relatively insignificant radiation hazard except in tissue, data on proton secondaries are valuable for checking against cross sections predicted by theories which treat protons and neutrons symmetrically. Strauch[2] has reviewed the forms of the secondary nucleon spectra expected and observed for reactions of nucleons near 100 MeV and above.

The cross sections discussed herein are defined for the production of a secondary proton in a specified energy and angle range, regardless of any production of other protons, neutrons, or gamma rays in the same reaction. If such a differential cross section, written as $\sigma_{p,xpy}(E;E',\theta)$ (ref. 3), is integrated over all secondary energies and solid angle, the result is

$$\int_{E'} \int_{\Omega} d\Omega \, dE' \, \sigma_{p,xpy}(E;E',\theta) = \nu_p(E) \, \sigma_{non}(E) ,$$

the product of the nonelastic cross section and the average multiplicity for production of secondary protons in nonelastic proton reactions at energy E. Unfortunately, because of spectrometer resolution inadequate for separating the elastic scattering, $\sigma_{p,xpy}(E',\theta)$ was not directly measured at small scattering angles in our experiment.

Preliminary results from this experiment [4,5] and from related secondary nucleon and gamma-ray experiments[6] in the same series are already available. The "telescope" experiments of Gibson et al.[6] in this series are comparable to those presented here, except that they have narrower

---

[2] A. K. Strauch, Measurements of Secondary Spectra from High-Energy Nuclear Reactions, TID-7652, Book 2, p. 409 (1962).

[3] C. D. Zerby and H. Goldstein, Neutron Phys. Div. Ann. Progr. Rept. Aug. 1, 1963, ORNL-3499, Vol. II, pp. 63-66.

[4] R. W. Peelle et al., p. 331 in Second Symposium on Protection Against Radiations in Space, NASA SP-71 (1965).

[5] R. W. Peelle et al., Neutron Phys. Div. Ann. Progr. Rept. Aug. 1, 1963, ORNL-3499, Vol. II, p. 73.

[6] W. A. Gibson et al., p. 331 in Second Symposium on Protection Against Radiations in Space, NASA SP-71 (1965); W. R. Burrus, B. W. Rust, and C. Schneeberger, Neutron Phys. Div. Ann. Progr. Rept. Aug. 1, 1965, ORNL-3858, Vol. II, p. 82; W. Zobel, F. C. Maienschein, and R. Scroggs, Spectra of Gamma Rays Produced by the Interaction of 160 MeV Protons with Be, C, O, Al, Co, and Bi, ORNL-3506 (1965).

energy resolution at the highest energies, do not extend to secondaries below 50 MeV, and were performed on a somewhat different selection of targets.

An incident 100- to 600-MeV nucleon is now conventionally thought to interact intitially with an effectively isolated target nucleon.[7] This view is rationalized by the incident nucleon's short wavelength and long pathlength in nuclear matter. Sometimes one or both nucleons will interact again, but if this does not happen, the reaction is thought of as a pure "quasi-free"* knockout scattering event. In either case, free-particle nucleon cross sections (n-p and p-p) are thought to dominate. If, however, the momentum transfer is very small, low-lying states of the residual nucleus are excited in what are generally considered nuclear rather than nucleon direct reactions.

When the sequence of quasi-free interactions is complete, it is often assumed that the nucleus may be deemed uniformly "heated" so that a nucleon evaporation process can occur, although Gugelot[8] and others have noted that equilibrium is a drastic assumption for an excitation attained through a simple primary interaction which generates a single deeply placed "hole." In any case, the residual nuclear excitation from such a primary process should be relatively small and a slowly varying function of the incident energy.

Low-energy-neutron spectra observed at various angles by Gross[9] at 190 MeV and proton spectra observed by Fox and Ramsey[10] at 160 MeV and by Bailey[11] at 190 MeV show, even for light targets, the qualitative

*"Quasi-elastic" has been much used in this regard as suggested in ref. 15, but recently has been widely employed for (p,n) reactions between isobaric analog states. "Quasi-free" seems more descriptive. "Knock-out" has been used at lower energies to describe reactions leading to low-lying residual states.

[7] Perhaps first suggested in the current context by R. Serber, Phys. Rev. 72, 114 (1947).

[8] P. C. Gugelot, p. 391 in Nuclear Reactions, Vol. I, P. M. Endt and M. Demeur, eds., North Holland Publishers, Amsterdam (1959-1962).

[9] C. E. Gross, The Absolute Yield of Low Energy Neutron from 190 MeV Proton Bombardment of Gold, Silver, Nickel, Aluminum, and Carbon, UCRL-3330 (1956).

[10] R. Fox and N. Ramsey, Phys. Rev. 125, 1609 (1962).

[11] L. E. Bailey, Angle and Energy Distribution of Charged Particles from High Energy Nuclear Bombardment of Various Elements, UCRL-3334 (1956).

features expected from evaporation spectra; they further found that the spectra are sufficiently independent of angle to be consistent with an evaporation model.

At the high-energy extreme of the emitted spectrum studies have been made of shape elastic scattering at 185 MeV,[12] 90 MeV,[13] and at 160 MeV.[14] Near-elastic reactions leading to low excited states have been studied at all available energies, limited mostly by resolution.

In the central regions of the emitted particle spectra, where quasi-free scattering appears at energies averaging a little below $E_o \cos^2\theta$,* broadened by the target nucleon momentum distribution as well as by failures of the quasi-free approximation, the data are qualitatively less consistent. Yet this region should contain a large share of the secondary energy, as well as a large share of the particles from light targets. At high energies and small angles the quasi-free peak was apparent in carbon in the experiment of Cladis, Hess, and Moyer,[15] who observed it at 30 and 40° for 340-MeV protons. Clean results have also been seen for outgoing protons at 650 MeV.[16] Quasi-free scattering is now usually studied in coincidence with reactions of the (p,2p) type.

Strong, broad, high-energy neutron peaks at extreme forward angles were seen by Randle et al.[17] at 160 MeV in elements as heavy as uranium, by Nelson, Guernsey, and Mott[18] at 240 MeV, and by Bowen et al.[19] at 143 MeV. In the cases of small momentum transfer, nearly elastic nuclear scattering may be confused with nucleon quasi-free scattering. All the forward-angle data except Bowen's suffered from the poor incident-energy resolution characteristic of recirculating cyclotron beams.

---

*Both relativistic effects and the average nuclear potential act to reduce the energy of any quasi-free scattering peak.

[12] A. Johnnson et al., Arkiv Fysik 19, 541 (1961).

[13] G. Gerstein, J. Niederer, and K. Strauch, Phys. Rev. 108, 427 (1957); A. E. Glassgold and P. J. Kellogg, Phys. Rev. 109, 1291 (1958).

[14] P. G. Roos, Elastic and Inelastic Scattering of High Energy Proton from Nuclei, Thesis, M.I.T. (1964). For elastic scattering, also see P. G. Roos and N. Wall, Phys. Rev. 140, 1237 (1965).

[15] J. B. Cladis, W. N. Hess, and B. J. Moyer, Phys. Rev. 87, 425 (1952).

[16] L. S. Azhgirey et al., Nucl. Phys. 13, 258-280 (1958).

[17] T. C. Randle et al., Phil. Mag. 44, 425 (1953).

[18] B. K. Nelson, G. Guernsey, and B. Mott, Phys. Rev. 88, 1 (1952).

[19] P. H. Bowen et al., Nucl. Phys. 30, 475 (1962).

Secondary protons observed in early experiments at 90° from 240-MeV protons incident on carbon[20] had an intensity strong enough and an energy high enough to confirm either the presence of very high momentum components in the nucleus if simple quasi-free scattering dominates or the importance of multiple-scattering effects. Quasi-free scattering characteristics have also been obscure in results at lower energies. Strauch and Titus[21] did not see evidence of them in the emerging proton spectrum at 90-MeV incident proton energy for any element at 40° or in carbon for any angle, though the near-elastic region appeared as expected. Similarly, Hofmann and Strauch[22] in studying neutrons from 90-MeV protons saw no quasi-free peak at any angle except for deuterium, beryllium, and lithium targets at small angles, and therefore were puzzled by why they should see no such peak in a light element when even uranium showed a quasi-free peak at 160 MeV in the work of Randle et al.[17]

Turning to the 150- to 160-MeV region directly of interest, nearly-elastic scattering has been studied, at least by Garron et al.[23] and Roos.[14] Roos also followed the quasi-free scattering for a number of elements until it approached his counter threshold of about 40 MeV, and found broad peaks for all elements and angles which terminated in the 50- to 60-MeV region. It will be seen that these data, which are supported somewhat by the work of Genin et al.[24] for gold and of Radvanyi and Genin[25] for carbon, are in conflict with the present experiment. Bailey[11] did not see such a cutoff in his spectra covering the 0 to 65° angle range.

Deuterons, tritons, and other particles have been seen in the emerging spectra since the earliest days. Hadley and York[26] at 90-MeV incident neutron energy made summations over angle to conclude that there were 30% as many deuterons as protons emitted for carbon and 18% for lead, with a disproportionately large share of deuterons emitted at angles below

---

[20] G. M. Temmer, Phys. Rev. 83, 1067 (1951).
[21] A. K. Strauch and F. Titus, Phys. Rev. 103, 200 (1956) and, 104, 191 (1956).
[22] J. A. Hofmann and A. K. Strauch, Phys. Rev. 90, 449 (1953).
[23] J. P. Garron et al., J. Phys. Radium 21, 317 (1960).
[24] J. Genin et al., J. Phys. Radium 22, 615 (1961).
[25] P. Radvanyi and J. Genin, J. Phys. Radium 21, 322 (1960).
[26] J. Hadley and H. York, Phys. Rev. 80, 345 (1950).

20°. On carbon targets Radvanyi and Genin [25] found about ten times as many protons as deuterons from 155-MeV protons for angles between 15 and 60°, with qualitative similarities in the shapes of the proton and deuteron spectra, and the data of Cooper and Wilson[27] are in essential agreement with this. Genin et al.[24] also found about 10% as many deuterons as protons at 155 MeV from a gold target -- a remarkable similarity with the carbon data. Roos[14] found a similar fraction of deuterons in pilot studies at 160 MeV. The deuteron spectra are usually conceived as combinations of direct and indirect pickup reactions, depending on whether or not the incident particle involved had already scattered.[28]

Detailed theoretical estimates of expected spectra have been obtained by the cascade-plus-evaporation model discussed in Section VI, combined with the optical model for elastic scattering. In the higher energy region and for favorable angles, Born approximation estimates on the basis of a single collision have also been made to relate the peak width of the quasi-free scattered spectrum to the nucleon momentum distribution.

While the present work suffers from poor energy resolution and lack of particle discrimination, it does combine spectra at several angles for targets other than carbon with carefully estimated energy response which reaches down to 20 MeV, lower than in other experiments responsive to the highest energy protons. The results bear on the question of the range of validity of the simple quasi-free model and its elaborations through the cascade-plus-evaporation model.

II. APPARATUS

The Basis of the Flight-Time Spectrometer

The differential cross sections reported here were obtained with the use of a flight-time spectrometer based on timing measurements with plastic and liquid scintillators. Figure 1 is a schematic view of the detector arrangement. The target and detectors were mounted in air, since in air 160-MeV protons lose only $\sim$ 1 MeV in the length of our apparatus and since the targets that were used are much ($\sim$ 20 times) thicker than the

---

[27] P. F. Cooper, Jr., and R. Wilson, Nucl. Phys. 15, 373 (1960).
[28] W. N. Hess and B. J. Moyer, Phys. Rev. 101, 337 (1956).

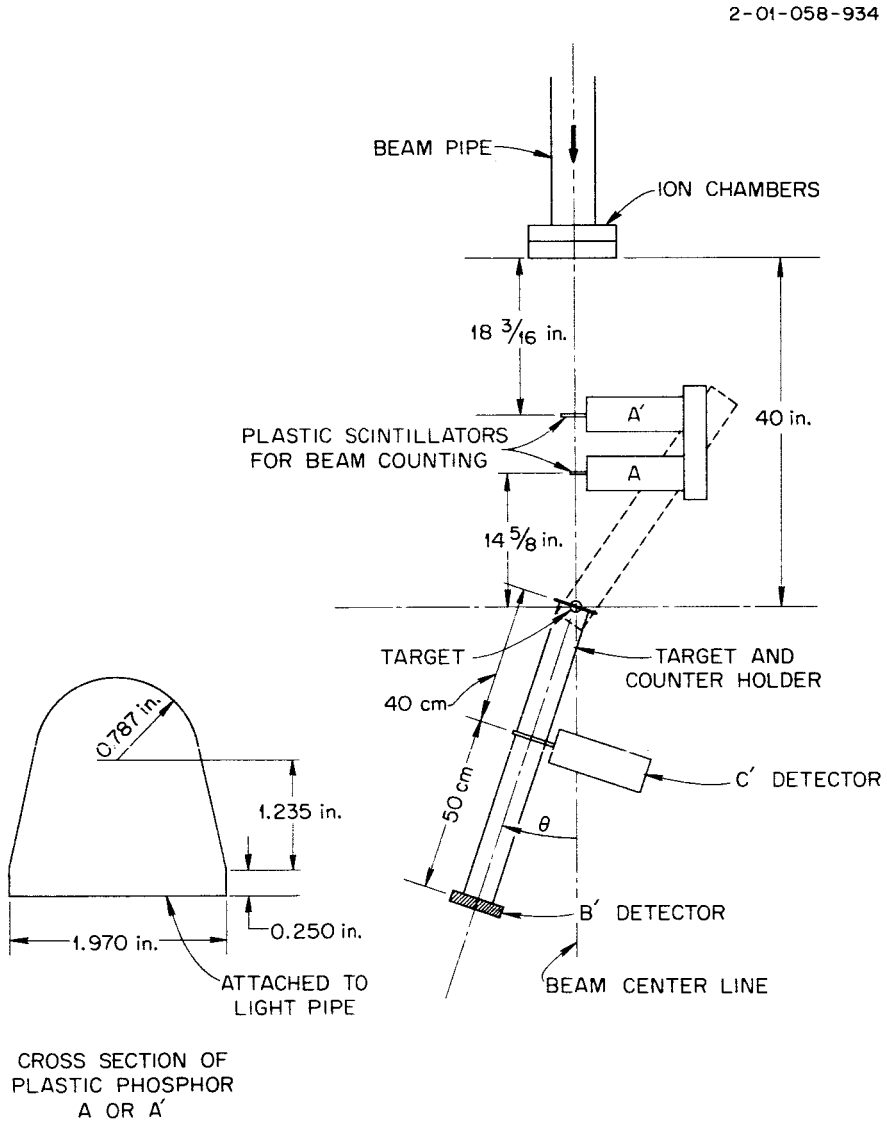

Fig. 1. Experimental Geometry for Proton Flight-Time Experiments, Including Cross Section of the 1-mm-thick A and A′ Beam Scintillators. A thin edge of counters A, A′, and C′ is viewed in each case by a 56-AVP multiplier phototube, while a flat side of counter B′ is viewed by a 58-AVP multiplier phototube.

amount of air that the secondary-proton detector is able to "see". These experiments were performed at a very low beam strength, specified below, so that there was only a small chance that two protons would appear in the beam within a $\sim$ 40 nsec rf period. This allowed counters A and A′ of Fig. 1 to detect individual protons. The flight time was measured between this detection of a primary proton and the occurrence of a pulse in counter B′. (Actually, a linear time base is initiated by the pulse in counter B′ and stopped by the corresponding delayed pulse from detector A.) A coincident pulse in the C′ detector is required if the flight time is to be recorded.

The flight paths used in these experiments were 90 and 70 cm, and a 150-MeV proton requires only 6 nsec to traverse the former flight path.

With the approximately 1-nsec resolution available, good energy resolution was not expected at the highest energies. At low energies the sensitivity was seriously compromised by energy loss in the apparatus. A proton leaving the target with 13 MeV could just be detected in counter B′, having just the 4-MeV energy at the detector needed to overcome the standard bias used. If this proton had originated in a reaction at the side of the target farthest from the detector, it would have started at about 25 MeV.

Definition of the Proton Beam

The properties of the beam of the Harvard synchrocyclotron have been described in some detail elsewhere,[29] and our use of it at low beam strength has also been discussed.[5,30] The cyclotron was adjusted to yield an average proton beam of about 5×10^4 protons/sec on the target, with an observed quadratic gross duty factor of about 2%. (If i is the current averaged over a period such as 10 μsec, the quadratic gross duty factor is defined[5] as $\bar{i}^2/(\overline{i^2})$.) Since the beam occurs only in short

---

[29] R. T. Santoro et al., Space, Time, and Energy Distribution of the Proton from the Harvard University Synchrocyclotron, ORNL-3722 (January 1965).

[30] R. T. Santoro and R. W. Peelle, Measurement of the Intensity of a Proton Beam of the Harvard University Synchrocyclotron for Energy-Spectral Measurements of Nuclear Secondaries, ORNL-3505 p. 38 (March 1964).

(1 to 4 nsec) pulses separated by the ~ 43 nsec rf period of the accelerating voltage, this implies on the average 0.12 incident protons per rf microburst during the gross (10^2 μsec) burst induced by the frequency modulation. However, the behavior of the machine was not so simple and regular as suggested by this average value.

As described[29] previously, the beam at the target was largely contained within a $\frac{1}{2}$-in.-diam spot generated by multiple Coulomb scattering in the ionization chambers used here for auxiliary beam monitoring. Beam position stability during the one-day intervals between adjustment was about 1 mm. The beam energy, based largely on range measurements,[29] was about 158.9 MeV as it entered the target, and so was approximately 158 ● 1 MeV at the point of interaction in a target 3 to 5 MeV thick, depending on the target angle. The beam energy spread during these experiments was dominated by this target thickness, since a study[29] of the experimental range curves places a limit of something like 1 MeV on the natural energy width of the incident beam.

In the paragraphs below are discussed the use of the coincident pair of counters, denoted by A and A′, to detect the presence of individual protons in the beam, determine their suitability for flight-time spectroscopy, and give the time of passage through counter A. These points were discussed in more detail previously,[5,30] partly in connection with a discussion of the calibration of the beam monitor ion chambers. To assure unambiguous identification of the flight time of an individual secondary, it was essential that only one proton pass through counters A and A′ during the time period required for a flight-time measurement. This "isolation interval" was set at 110 nsec, implying that two rf-induced fine-structure burst positions on either side of one position containing an acceptable proton had to be "empty." Pulse pileup events, wherein two or more protons occupied the same fine-structure burst position, also had to be rejected because they would tend to degrade the time resolution of the system if the fine-structure bursts were wider than 1 nsec.

Figure 1 shows the beam counter geometry, and Fig. 2 the block diagram of the overall-beam-handling apparatus. The two thin scintillation counters A and A′ are shown to be interposed in the proton beam

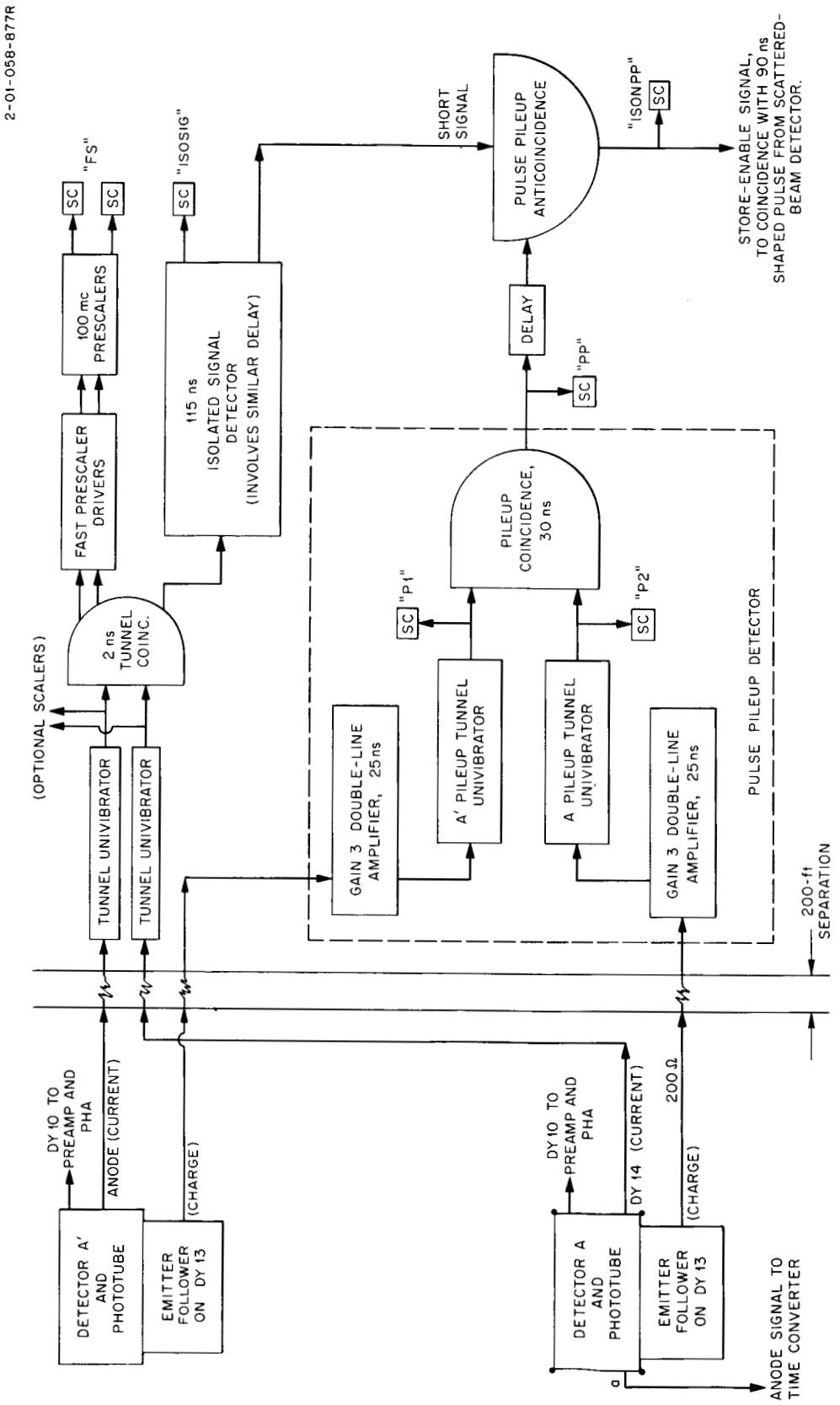

Fig. 2. Block Diagram of Beam-Handling Apparatus. Variable delays to assure synchronization are not shown. The tunnel univibrators act as fast integral pulse-height discriminators. The symbol SC stands for a 10-mc scaler, and the mnemonic name of the resulting count is in quotes.

before it struck the target. (The counters were designed by V. McKay and H. Brashear of the Instrumentation and Controls Division, as were all the detectors used in these experiments.)

The properties of the nanosecond circuit elements used throughout the electronic apparatus have been described by Hill et al.[31] The outputs of the counters were coupled by a pair of independent coincidence and logic systems. The faster system (designed largely by N. W. Hill, Instrumentation and Controls Division) used current pulses from the photomultipliers and was capable of responding to closely spaced coincidences (10 nsec), later rejecting any events in which two protons were spaced by less than the preset "isolation" interval. The other system (designed largely by R. J. Scroggs, Instrumentation and Controls Division), labeled in Fig. 2 as "Pulse Pileup Detecting" used charge pulses and employed discriminators and a second coincidence circuit to recognize pileup events. Provisions were made to record the number of pulses reaching each important point in the circuit.

Figure 3 shows a comparison of the charge spectrum of pulses from detector A, for a beam strength of a few hundred protons per second, with the energy-loss distribution estimated by using the formulation of Symons.[32] The points show the observed pulse-height spectrum with the pulse-height scale normalized to give the predicted mean energy loss, neglecting data above 0.9 MeV. Curve A is the normalized predicted energy-loss distribution folded with a normal distribution to represent the detector resolution. The standard deviation of the normal distribution was chosen by comparing the second moments of the energy-loss spectrum and the portion of the data below 0.9 MeV. Above 0.9 MeV the experimental distribution has greater intensity than the predicted one.

As shown in Fig. 2, fast current pulses from detectors A and A′ were fed to tunnel-diode univibrator discriminators biased at a detector energy loss of 150 to 200 keV. A tunnel-diode coincidence circuit with a 2-nsec resolving time determined that a given proton had passed through

---

[31] N. W. Hill et al., Performance Characteristics of Modular Nanosecond Circuitry Employing Tunnel Diodes, ORNL-3687 (1964).

[32] K. R. Symons, Fluctuations in Energy Lost by High Energy Charged Particles in Passing Through Matter, Thesis, Harvard University (1948).

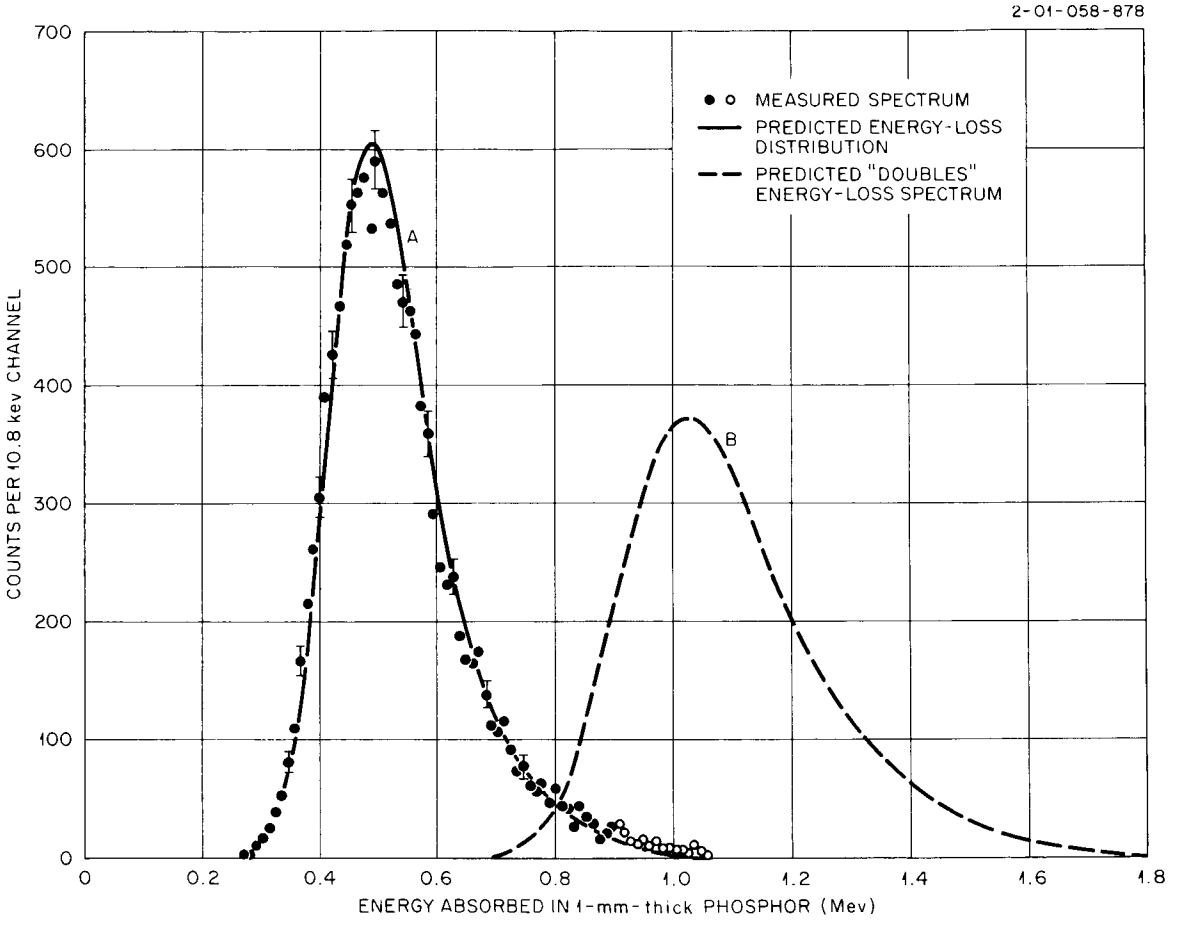

Fig. 3. Comparison of Pulse-Height Spectrum from a 1-mm Plastic Phosphor Scintillator Penetrated by 160-MeV Protons with a Smeared Predicted Energy-Loss Distribution.

both counters. Delayed coincidence curves such as those in Fig. 4 suggest[33] that this circuit usually operated with a coincidence efficiency well in excess of 99%. The dead time of the univibrators was about 10 nsec; so two protons in the same rf microstructure burst were not resolved, while those accelerated in successive rf periods always generated coincidence outputs. The scatter in the experimental points in Fig. 4 is believed to have been caused by small inaccuracies in some of the delay cables used.

It was necessary for the pulses from this fast (AA′) coincidence to survive the isolated signal system and the pulse pileup anticoincidence in order for any detected secondary particle to be stored. The isolated signal system shown in Fig. 5 was constructed using tunnel-diode circuit elements and was adjusted to eliminate from a train of pulses any pairs or multiples falling within 110 nsec of each other. In the limit of no dead times or circuit delays, the synchronizing delays D_1, D_2, and D_3 would be unnecessary and the pulse storage delays would be set at the desired isolation interval (110 nsec in this case). A naturally isolated input pulse fired both binaries and reset them at the end of the isolation time, giving an output via the "trailing edge coincidence." If two pulses were too closely spaced, the second pulse was eliminated because binary I could not be reset by the second pulse when the first had already reset it, and the first pulse was eliminated by the second through the early reset of binary II, via the "reset coincidence." Practical circuit delays were important, binary dead times were about 5 nsec, and the reset and output coincidence circuits had a resolving time of about 3 nsec. Circuit behavior with more complex pulse trains is difficult to describe, but the instrument was tested with quadruple pulses. While the logic illustrated in Fig. 5 is believed to be adequate, the resolving times of the included coincidence circuits sometimes caused malfunctions of the equipment during the relatively infrequent pulse trains having pulses in four or more successive fine-structure bursts.

The pulse pileup detector (lower center of Fig. 2) was used to identify those rf periods in which two or more protons occurred. The

---

[33] R. W. Peelle, Nucl. Instr. Methods 29, 293-298 (1964).

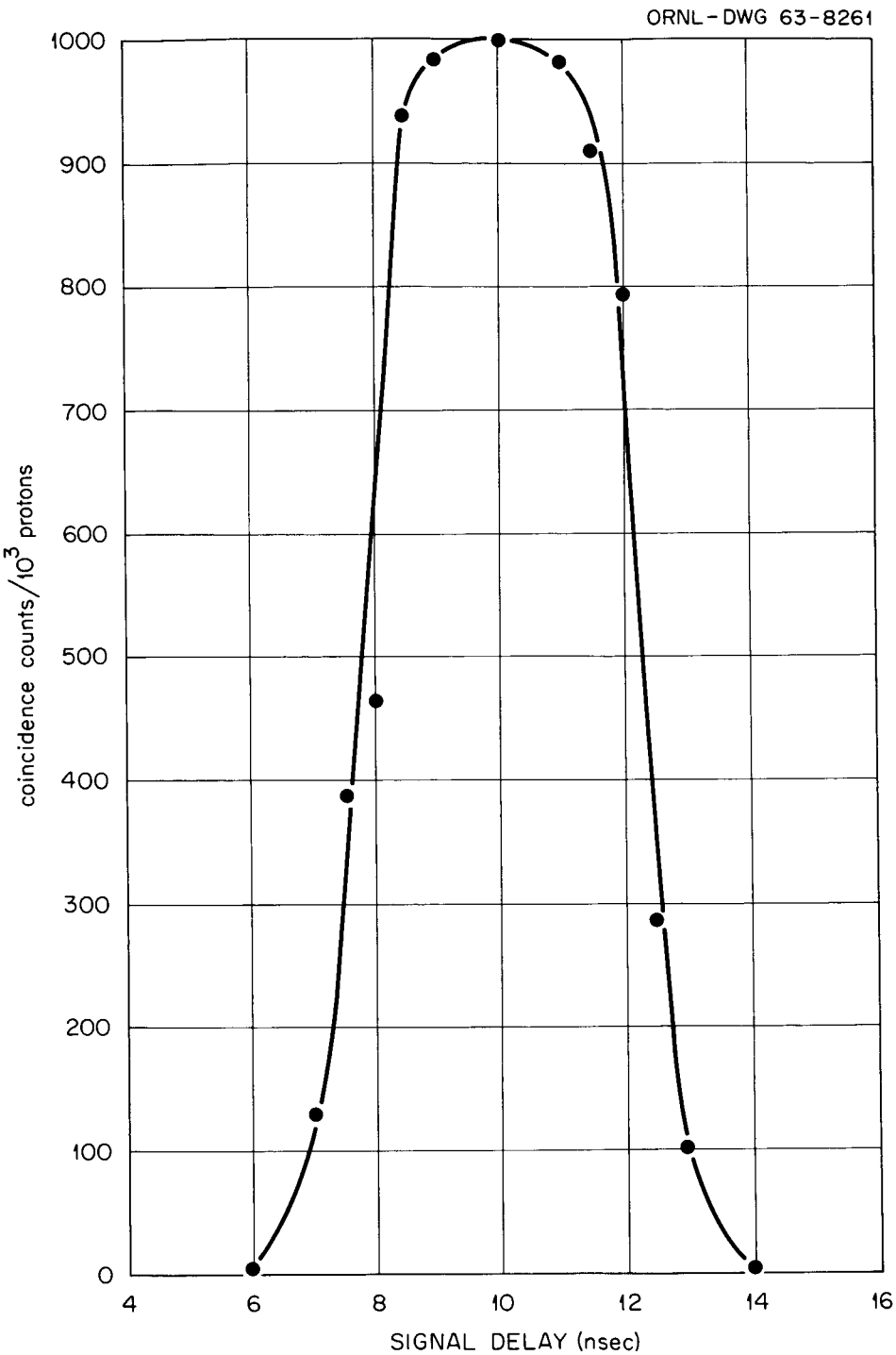

Fig. 4. Delayed Coincidence Curve for the Beam Scintillators. The slopes at the sides of this curve and the zero count rate observed at abscissae two resolution widths from its center suggest 100% counting efficiency.

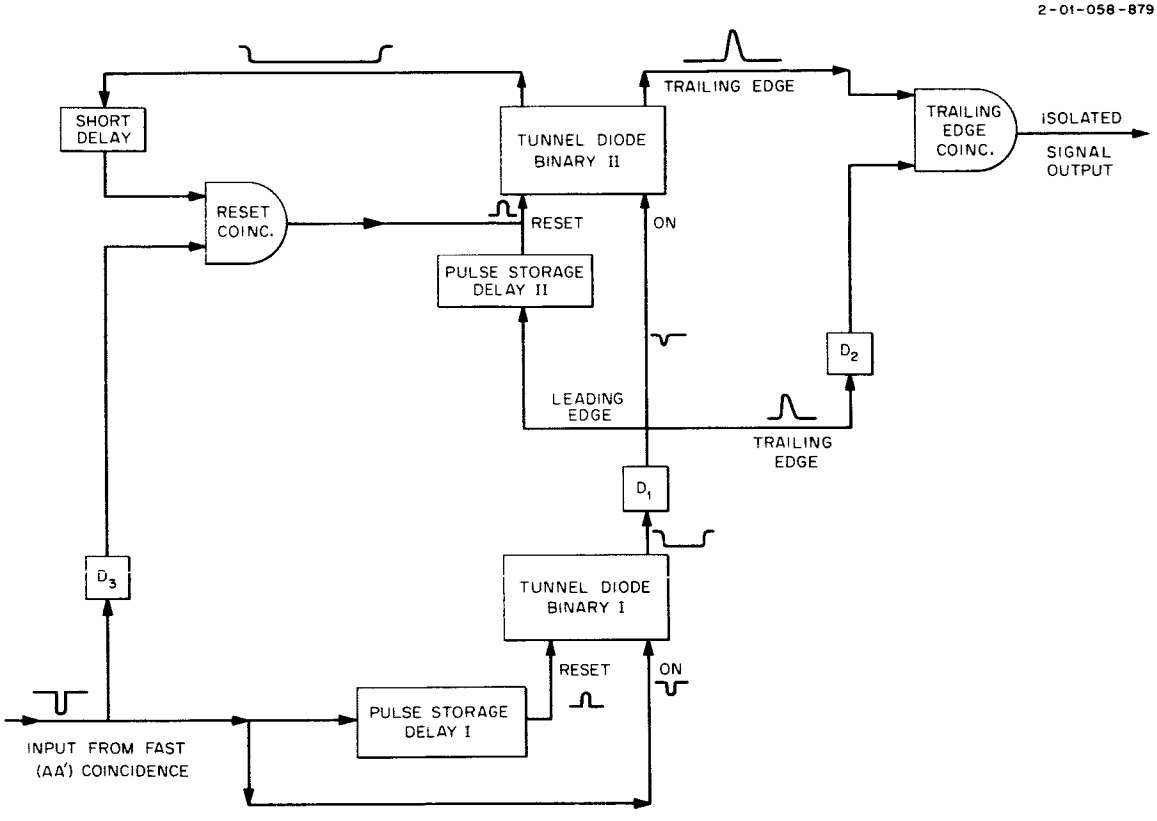

Fig. 5. Block Diagram of Isolated Signal Detector.

input charge pulses were double-delay-line clipped using 25-nsec lines so that protons too close together to be resolved by the fast scaling system would appear as one large pulse. Assuming that the beam detector introduced a variance proportional to the energy loss in the phosphor, Fig. 3 shows an estimate of the distribution of pulse heights which should result from "double" events involving two protons in the same fine-structure interval (curve B), based on the observed resolution for single events and the predicted energy-loss distribution for two protons simultaneously penetrating 1 mm of plastic phosphor. No experimental data could be obtained for comparison, but oscilloscope observations tended to confirm the analysis. Figure 3 also shows that no pileup discriminator setting can effect a complete separation of single and pileup events, but the distributions shown can be integrated to obtain for each detector (A and A′) a relation between singles and pileup efficiencies such as that shown in Fig. 6. To overcome the inadequate resolution of individual detectors, the pileup discriminators on both A and A′ channels were set for single-event counting efficiencies of about 0.03, and the discriminator output signals were placed in coincidence. The efficiencies at the output of the pileup coincidence circuit are roughly the square of the individual values; so an overall pileup detection efficiency of about 90% could be maintained while counting only 0.1% of the single events. The entire pileup discriminator and coincidence system was built with longer dead times than the fast coincidence system, allowable because the discriminators were set to count less than one-tenth of the proton pulses. The input circuitry had to be capable of handling the full rates without appreciable base-line and gain shifts.

As far as the spectroscopy of secondary radiations was concerned, the only important pulses were those which appeared as "isolated" signals and which were not recognized as pulse pileups. Others did not lead to a recorded time interval and were not recorded in the ISONPP scaler as being part of the beam. The remaining scalers associated with the beam-handling apparatus were employed to assess the reasonableness of the operation of the equipment, to help calibrate the beam monitor ion chambers, and to provide a certain redundancy of information in case of

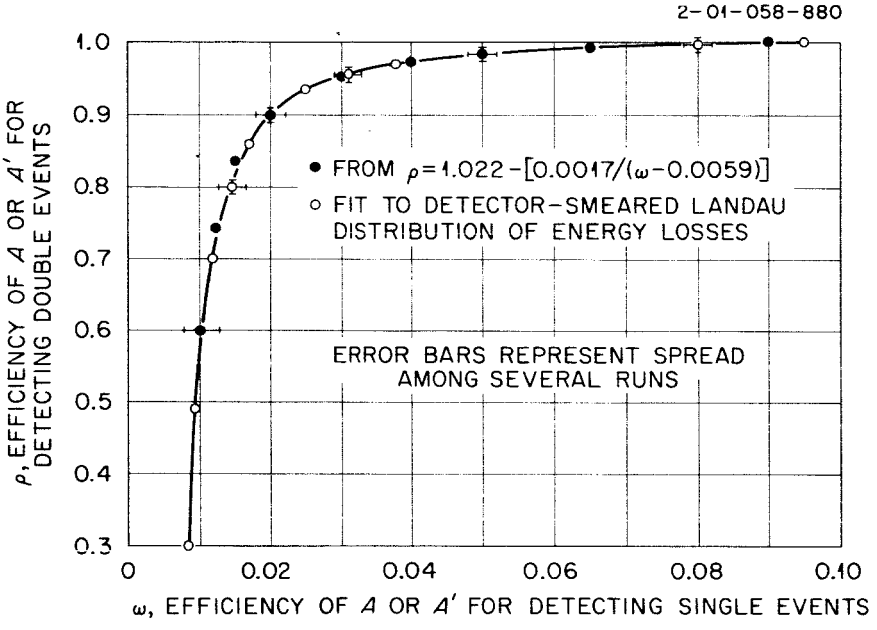

Fig. 6. Estimated Relation Between Efficiencies for Counting a Pulse from One (ω) or Two (ρ) Protons in a Given Beam Microburst. The points along the curve would be obtained as pileup discriminator A or A′ is adjusted.

failure of a scaler. Use of the apparatus for these auxiliary purposes is detailed elsewhere.

The Telescope for Secondary Protons

In order to be detected, a secondary charged particle had to penetrate detector C′ of Fig. 1 (0.05 cm of plastic phosphor, 4 in. in diameter, covered by 6 to 10 mg/cm^2 of Aℓ), traverse an air path of 30 to 50 cm, and finally enter detector B′ (0.5- by 5-in.-diam plastic phosphor, covered like C′). These components formed the secondary-proton telescope, with a (B′C′) coincidence required to identify charged secondaries. The detection bias on the fast component of the pulse from B′ was set at a value corresponding to a 1.3-MeV electron; a 4-MeV proton should produce the same amount of light.

A (B′C′) delayed-coincidence test curve obtained during the experiment is displayed in Fig. 7. The random coincidence rate with the 24 nsec (2τ) resolving time is estimated to have been less than 1% of the true coincidence rate in all cases, and in turn only a few of these random events could have come in the proper time relation to a beam proton. The curve shown in Fig. 7 was obtained by using 160-MeV protons from the beam, and implies a coincidence efficiency of about 98% at the point noted for the standard setting. The timing becomes more favorable for protons of lower energy, and the time corresponding to the slowest proton detected is shown approximately in Fig. 7.

Noise dominated the ungated spectrum of total-light pulses from detector C′; Fig. 8, however, shows spectra from detector C′ in coincidence with pulses in detector B′ and in coincidence with a signal from the beam counters, both produced by the 160-MeV proton beam passing sequentially through the center of each detector. The general agreement between the spectra is taken to imply that the threshold on the fast current signal from C′ was set sufficiently low to count all protons. Larger pulses were observed from protons of lower energy or those striking detector C′ away from its axis. By contrast, the pulse distributions in detector B′ from monoenergetic protons were clean and unambiguous, though protons striking the periphery of the counter's face produced pulses 20% smaller than those produced by protons striking near the

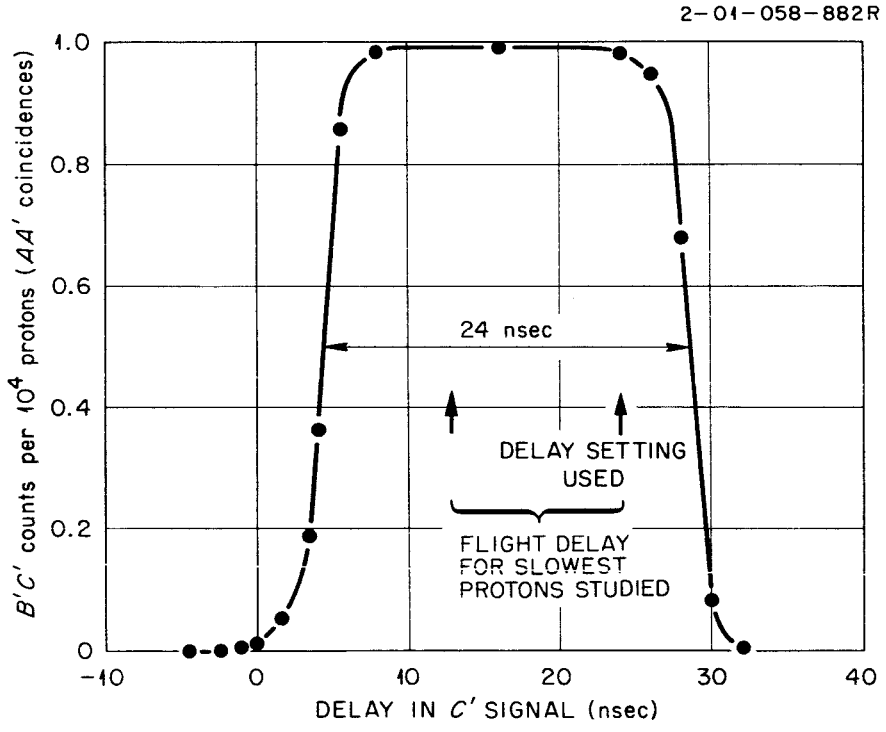

Fig. 7. Delayed Coincidence Curve for the (B′C′) Coincidence System Using 160 MeV Protons, with 30 cm Separating the Two Counters. The curve is required to be this broad because of the wide energy range of the protons traversing the path between the counters.

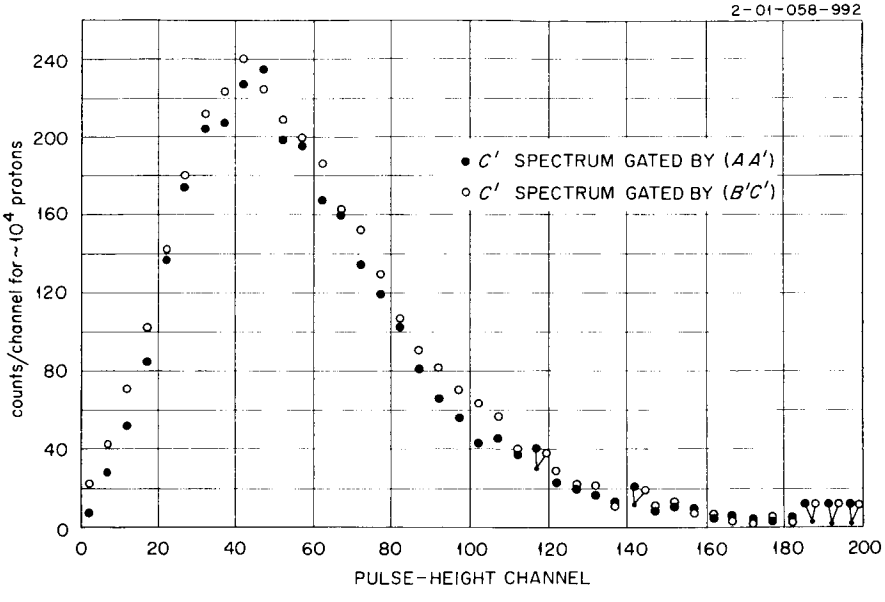

Fig. 8. Gated Total-Light Spectra from Detector C′ for Protons Striking the Center of the Counter. Note that the spectrum seems little modified by the C′ threshold discriminator.

center. Figure 9 illustrates the total-light pulse distribution for protons striking the center of the face of detector B′.

The telescope described did not provide much protection against detection of secondary charged particles other than protons, but did provide sure discrimination against neutron and gamma-ray detection through the thinness of C′ and the spacing of it from detector B′. A deuteron from the target which could reach B′ would have counted in the (B′C′) coincidence circuit. This difficulty is serious because of evidence from other work[14,24-28] that deuteron production is sometimes important. Considering the energy losses in the apparatus and the target, various particles would have been detected as shown in Table 1. The bias thresholds in detector B′ for the various particles and the equivalent proton energies were approximated very roughly.

The angular resolution of the telescope was governed by the geometry of the detector and by multiple scattering, largely in the target. All runs for 10 and 30° scattering angles were made with the 12-cm-diam detector about 90 cm from the target, while runs at wider angles were made at a 70-cm distance. In nearly all cases this ± 3 or 4° angular spread dominated the resolution. However, for the lowest energies observed the resolution was effectively increased by the multiple Coulomb scattering in the target material. Table 2 lists the approximate rms (projected) scattering angles for the lowest secondary proton energies important in each of the first few energy bins for various targets. The table includes only cases for which the estimated rms multiple-scattering angle is greater than the geometrical rms scattering angle of 0.03 radian (for the appropriate 90-cm flight path). For greater scattered energies, lighter target materials, or shorter target-to-detector distances the geometrical resolution given above becomes increasingly dominant. The values in Table 2 were actually computed for secondary particles originating in the center of the targets for secondary proton energies chosen at the lower edge of each energy bin included.

The overall detection efficiency of the telescope was close to unity for those protons which left the target toward any point in detector B′, corresponding to the solid angle used in obtaining zero-order cross sections. The various possible disturbing effects were canvased to

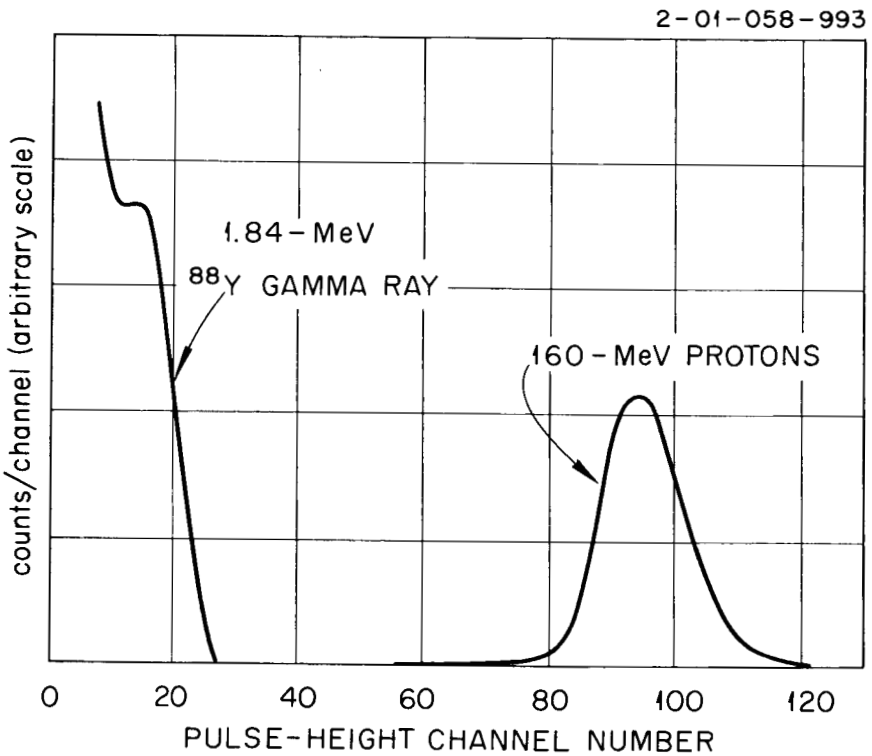

Fig. 9. Pulse Distributions from Detector B′ for Incident Gamma Rays from ^{88}Y and from 160-MeV Protons Striking the Counter Perpendicularly at the Center of Its Face. These protons lose about 6.0 MeV in detector B′.

Table 1. Detection Ranges for Particles Other Than Protons in the Secondary Charged Particle Telescope for a 0.5 g/cm^2 Carbon Target with Its Normal Toward the Detector.

Particle Type	Minimum Energy for Detection (MeV)	Energy of Equivalent Proton[a] (MeV)	
		Particle at Minimum Energy	Particle at 160 MeV
Proton	12.6 - 25		
Deuteron[b]	21 - 36	12.6 - 25	78
^{3}H[b]	30 - 46	12.6 - 25	51
^{3}He	44 - 88	13.2 - 26	48
^{4}He	50 - 100	12.3 - 25	35

[a]For each particle and energy the "equivalent proton" would yield pulses in the same time region for a 90-cm flight path. Where a range of energies is given, the two values refer to secondaries produced at the front and the rear of the target; otherwise, the energies refer to secondaries produced at the target midplane.

[b]In these cases the threshold is determined by the maximum flight-time considered, while in the remaining cases the detector threshold governs.

Table 2. Estimated r.m.s. Projected Multiple Coulomb Scattering Angle from Target-Scattering for Typical Runs at 30° Scattering Angle, Assuming a Normal Angle Frequency Function.

Target Material	Bin Energy (MeV)	Energy of Protons Leaving Target (MeV)	r.m.s. Projected Multiple Scattering Angle (radian)
Bi	20.6	13.2	0.13
	27.2	21.5	0.09
	35.6	31.0	0.07
	48.8	40.0	0.036
Co	21.5	13.1	0.08
	29.4	23.5	0.05
	38.2	33.0	0.036
Aℓ	20.8	13.1	0.053
	28.6	22.5	0.031
C	21.5	13.2	0.033

determine which caused efficiency degradation by as much as a fraction of a percent. A rough energy dependence was estimated for each significant effect. For each run a table of the combined efficiency factors was consulted in order to make an energy-dependent correction. A list of the correctable items follows:

1. Analyzer counting losses amounted to from 0.14 to 2.2%, no energy dependence.

2. Nonelastic interactions in the target weaken the primary beam from 0.2 to 0.5%. The secondary beam suffers an energy-dependent absorption in the target, from 0.2 to 0.5% at highest energies up to 0.3 to 1.6% at lowest energies.

3. Nuclear scattering in the components of the telescope varied from 1.3% for 20-MeV secondaries to 0.7% at 60 MeV and 0.5% at 160 MeV.

4. (B′C′) coincidence losses were estimated to vary from 0% below 40 MeV to 1% at 100 MeV and to 2% above 140 MeV.

5. Multiple scattering in detector C′ was most serious in the data obtained at 10°, and is estimated to have produced losses there up to 1.7% in the lowest energy bin. The correction was half this large for the 30° data. In both cases at 30 MeV and above the correction is below 0.2%.

The combined corrections from the above sources ranged from 2 to 5%. An overall uncertainty of 1.5% in efficiency was assigned to cover the combined correction, but was not assigned an energy dependence.

Flight-Time Measurement

Flight-time measurements were made using a time-to-pulse-amplitude converter designed by F. M. Glass (Instrumentation and Controls Division). As our other fast circuitry, this unit employed tunnel diode input univibrators as timing circuits. The $\sim \frac{1}{2}$ μsec pulse at the output had its amplitude linearly related to the time difference between "start" and "stop" inputs. The integral long-range linearity and stability of the unit were good, but the differential linearity proved to be troublesome. Figure 10 shows a differential linearity curve (obtained using random "stop" signals) which illustrates the difficulty. The solid parts of the curve refer to the time range employed in this experiment. Baseline

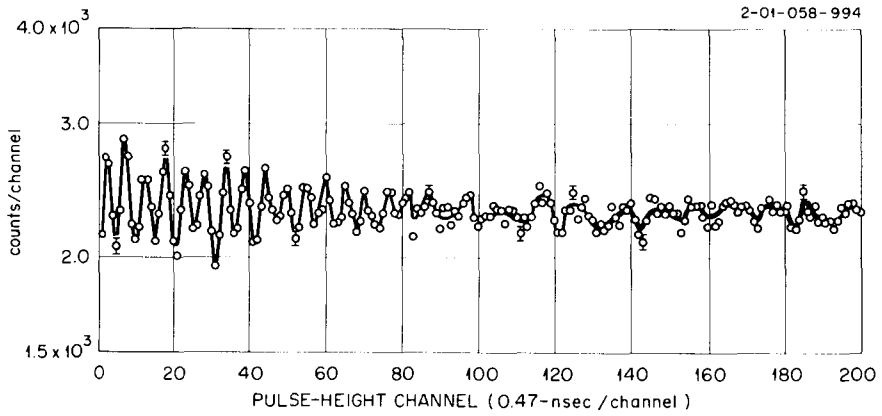

Fig. 10. A Typical Differential Linearity Curve Obtained by Using Random Start and Stop Pulses into the Time-to-Pulse Height Converter. The fluctuations were ignored in the analysis of the data, which only involved the portions of the curve from channel 130 through channel 190. Aside from counting statistics, the ordinate for a given channel is proportional to its true time width.

stability was adequate for these proton results, although the shift of ~ 0.0005 nsec/cps produced difficulty in other experiments.

In all cases "zero" time was deduced from observations of the apparent flight time of beam protons through the apparatus with the detector placed at zero degrees and the cyclotron beam intensity adjusted to about 500 protons/sec. Drifts of this time "zero" were about 0.2 to 0.3 nsec over a series of runs requiring a few hours. Figure 11 illustrates such a timing check, as well as the system's integral linearity, and exhibits a time resolution of about 1 nsec for 160-MeV protons.

The overall conversion gain of the timing equipment was 0.468 nsec per channel ± 1%, based on examination of the results obtained by two independent techniques: One technique was based on differential linearity tests, such as that plotted in Fig. 10 which can yield an absolute measure of conversion gain provided that the "start" and "stop" rates are measured and all counting difficulties such as dead times are considered. A series of such runs under varied conditions implied conversion gains in the range 0.466 nsec per channel ± 0.3%. The other involved carefully cut RG9BU delay cables which yielded a calibration depending upon manufacturing tolerances on the signal velocity in the cable. Depending on the velocity value chosen, the delay cable yielded a conversion gain of 0.471 nsec per channel, with an estimated uncertainty of 0.5%. The uncertainty on the chosen value seems generous, but it has little effect on the overall error estimates. All timing checks implied the same conversion gain within ± 0.5%. The time resolution and calibration data discussed above and shown in Fig. 11 all employed a pulse distribution such as that shown in Fig. 3 for counter A and in Fig. 9 for counter B′.

To assume that the B′ pulse distribution is constant would be inadequate because there was a pulse amplitude dynamic range of at least 10:1 in counter B′ within the useful parts of the time spectrum. Figure 12 shows the relation between the light output from counter B′ and proton energy at the face of that counter. The light output per absorbed MeV was taken from the work of Evans and Bellamy.[34] The peak

[34] H. C. Evans and R. H. Bellamy, Proc. Phys. Soc. 74, 483 (1959).

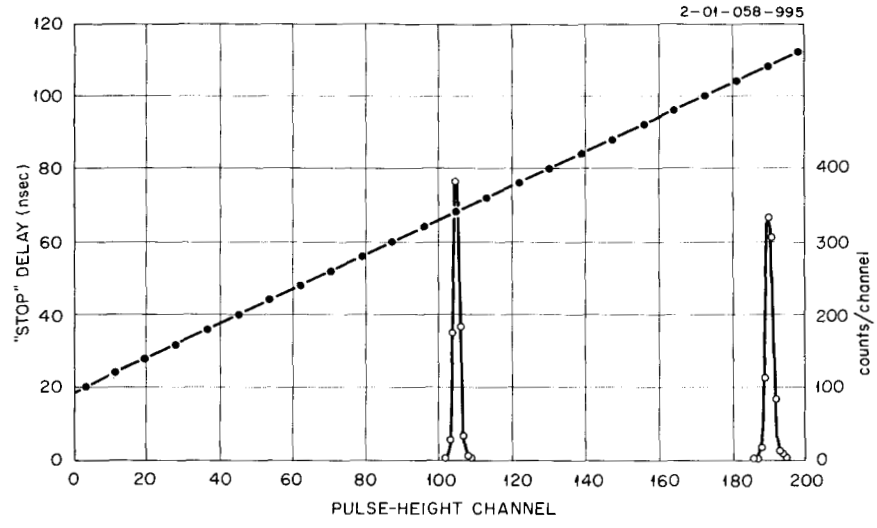

Fig. 11. Operation of the Time-Measurement System for Monoenergetic Protons in the Unscattered Beam. The observed resolution width is slightly under 1 nsec for such timing checks (right-hand ordinate scale). The typical long-range integral linearity curve seems linear to a small fraction of 1% in the interval illustrated. Very detailed integral linearity checks showed fluctuations corresponding to those observed in the differential check in Fig. 10.

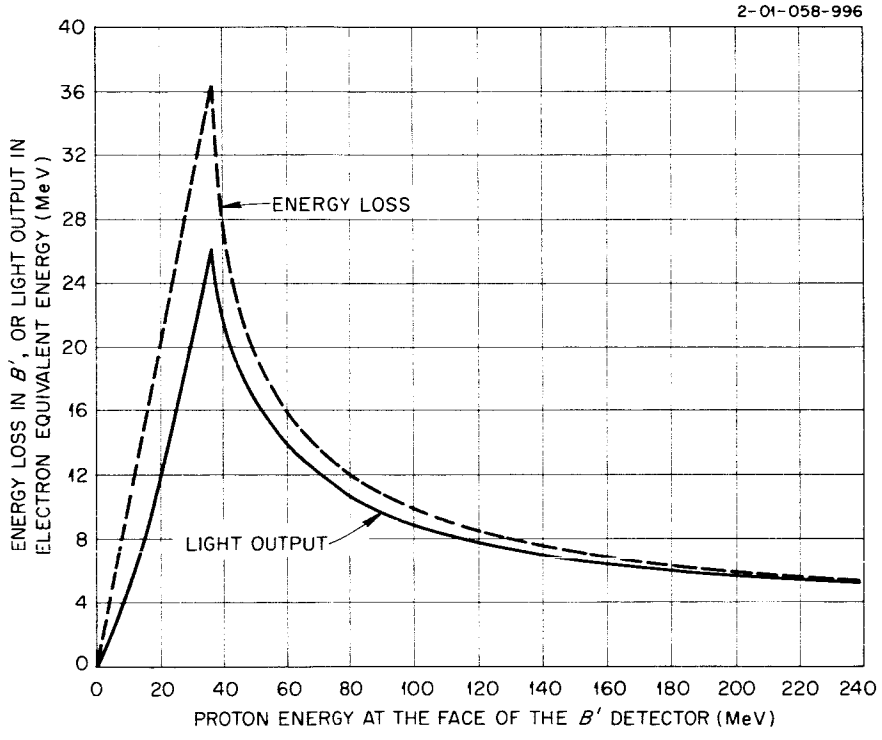

Fig. 12. Energy Loss and Electron-Equivalent Light Output for Protons Penetrating the Surface of Detector B′ ($\frac{1}{2}$-in. Polystyrene-Based Phosphor).

at about 38 MeV corresponds to the energy for which the proton range in polystyrene-based plastic phosphor is just the 0.5-in. counter thickness. Figure 13 illustrates the pulse amplitude dependence of the time measurement with the equipment used, for a constant time between physical events. The closed-circle points were obtained using degraded 160-MeV protons, while the open-circle data were matched on from data obtained a year later using the same electronics similarly adjusted, a 1- by 5-in.-diam liquid scintillator detector, and pulse pairs obtained in the detection of alpha particles and their associated neutrons from the $T(d,n)^4He$ reaction.[35] The amplitude-dependent timing walk (or slewing) is plotted here as a function of "overdrive," the ratio between the amplitude of the fast current pulse and the minimum pulse capable of firing the tunnel univibrator at the input to the time-to-amplitude converter. It was necessary to choose an arbitrary time zero in matching the two sections of the data. A combination of the results of Figs. 12 and 13 yields the final timing "walk" curve of Fig. 14, in which the major uncertainty is the exact B′ pulse-height threshold employed during some of the experiments at the "stop" input of the time-to-pulse-height converter. It is seen that quite substantial corrections were required near 40 MeV, where the overall flight time was 10 to 12 nsec. In all these studies the pulse spectrum from detector A into the "stop" input of the time-to-amplitude converter was held fixed, while the apparent time difference between "start" and "stop" pulses was observed for various energy losses in detector B′.

The data of Fig. 14, fitted with the illustrated straight lines, were employed directly in the data analysis to convert the difference in time between observed pulses into an inferred time difference between events. This was possible because each apparent flight time corresponded to a narrow band of energies at the face of detector B′. The error in the timing walk correction was taken as 25% of the difference from the value at 158 MeV, where the routine timing checks were performed during the experiment.

---

[35] T. A. Love et al., Absolute Efficiency Measurements of NE-213 Organic Phosphors for the Detection of 14.4 and 2.6 MeV Neutrons, ORNL-3893 (in preparation).

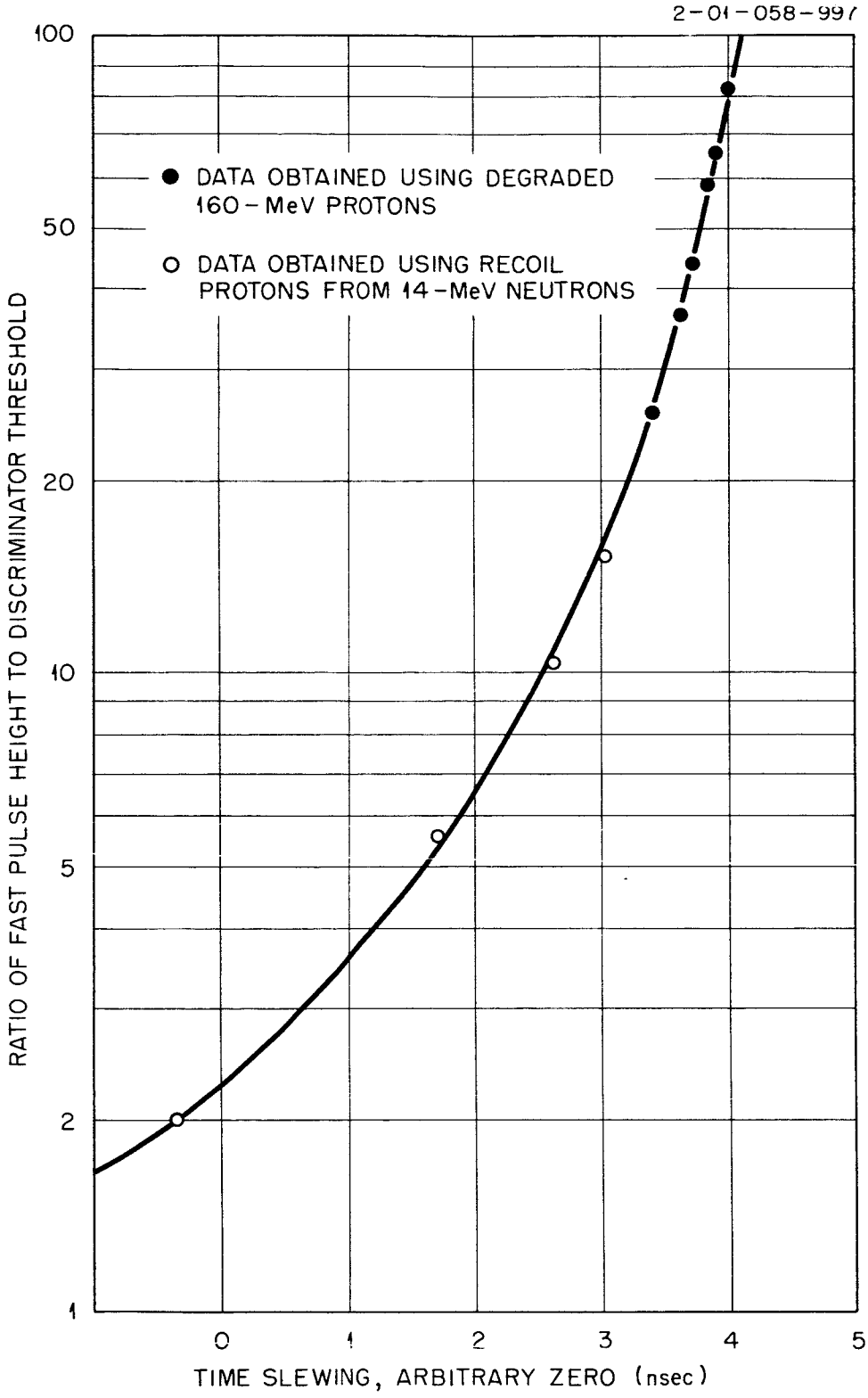

Fig. 13. Time Slewing for the Secondary Proton Detector. Note that the time scale appears to be reversed because the detector is attached to the START circuit of the amplitude converter.

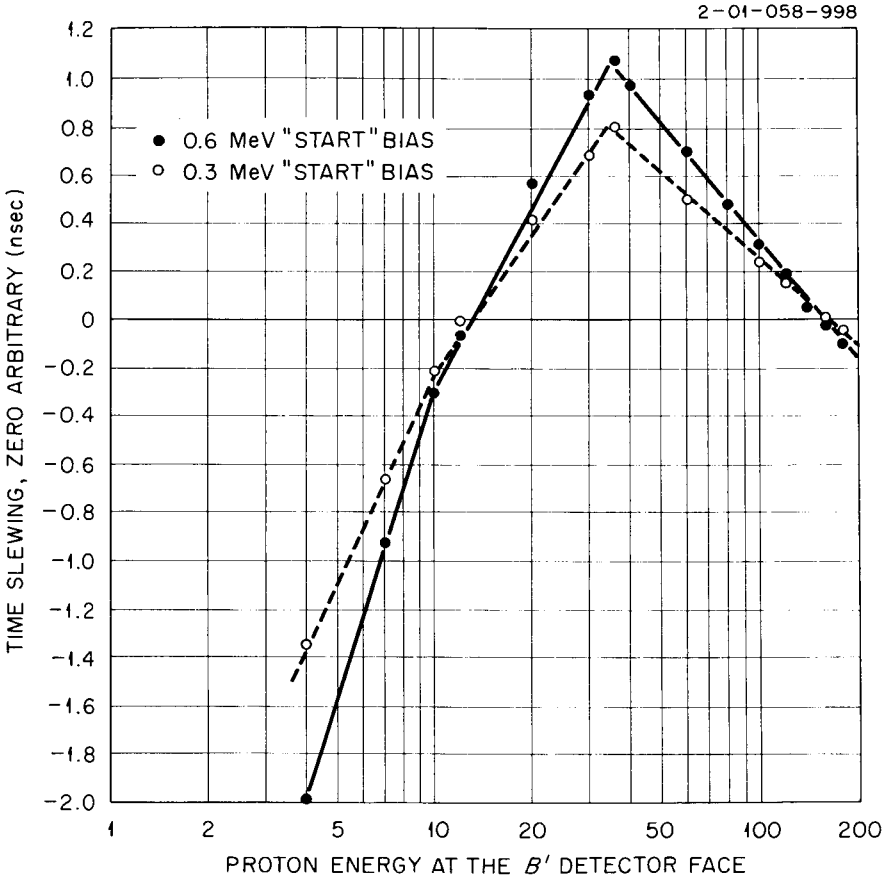

Fig. 14. Time Slewing as a Function of Proton Energy at the Face of Detector B′. Results are shown for two values of the pulse-height threshold at the input to the time-to-pulse-height converter, normally set at about 0.6 MeV electron equivalent.

The Supervisory System

Figure 15 is a schematic flow diagram of the overall electronic system, showing the interrelation of the beam-processing package, the telescope (B′C′) coincidence circuit, and the time-to-amplitude converter through the slow gating circuit to the information storage in the multichannel pulse-height analyzer. This gating and storage is so arranged that if an event meets all conditions for storage except a telescope (B′C′) coincidence the flight time will be stored in a separate section of the analyzer memory.

In summary, the following conditions must be met if a flight-time observation is to be stored:

In the Beam Package:

1. Simultaneous (± 2 nsec) pulses arise in counters A and A′, with amplitudes > 150 keV-equivalent.
2. No other coincident pulse appears within 110 nsec of the one of interest.
3. Both A and A′ do not register pulses above their pulse pileup discriminator thresholds.
4. The observed secondary particle occurs within a reasonable interval (-10 nsec, + 80 nsec) of the proton pulse from counter A.

In the (B′C′) Coincidence Circuit:

1. The pulse observed in detector B′ has a light output greater than would be produced by an electron of ~ 1.3 MeV.
2. The pulse in detector B′ follows within 25 nsec that observed in detector C′ with bias equivalent to > 100 keV.

In the Time-to-Amplitude Converter:

1. All pulses which exceed the threshold of circuits B′ and A yield a time-to-amplitude conversion provided that neither is spaced within the dead time of ~ 60 nsec from the preceding pulse. If no beam timing pulse accompanies a B′ pulse which is above the "start" threshold, the converter yields a large "self-stop" pulse.

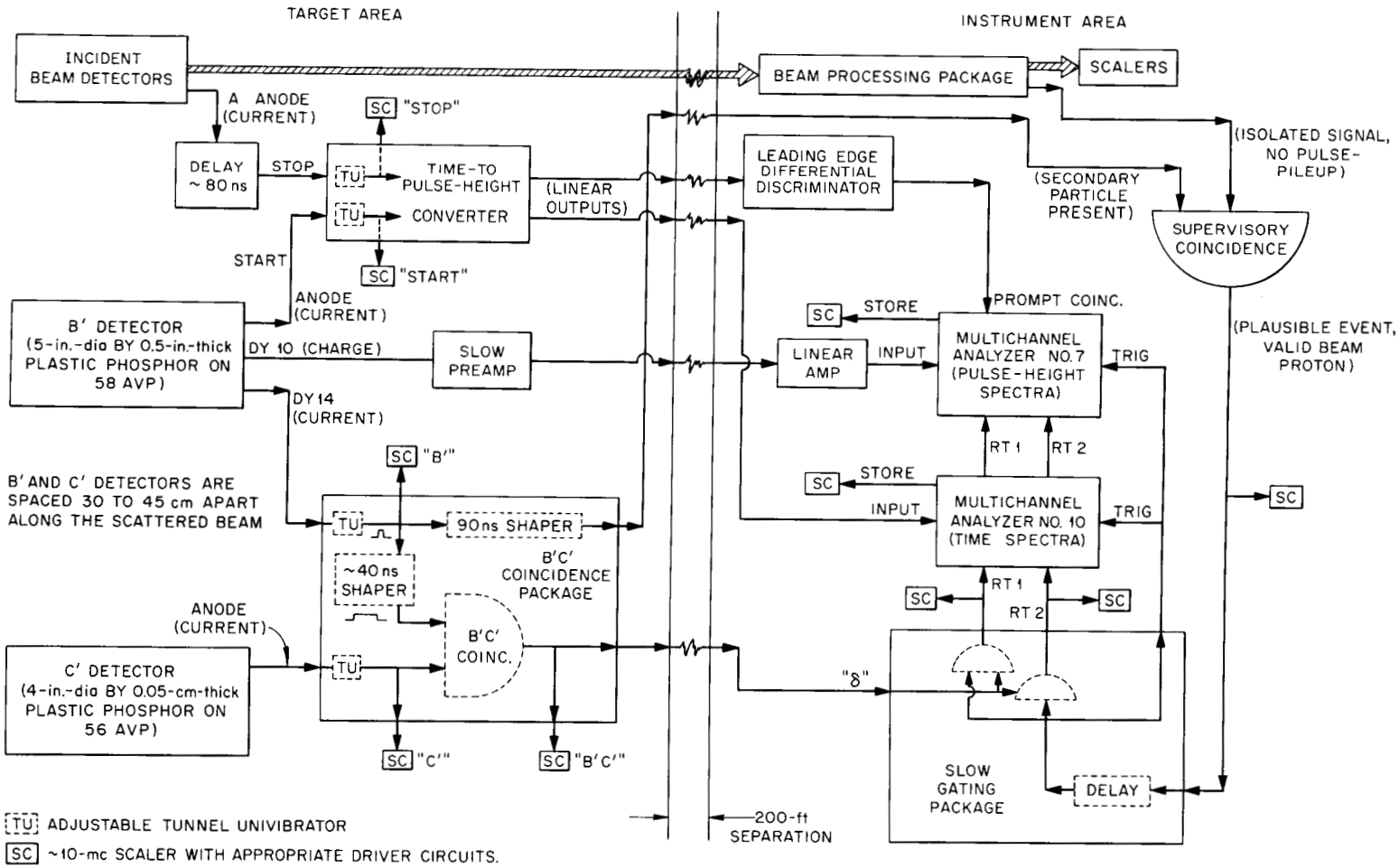

Fig. 15. Electronics for Charged-Particle Flight-Time Spectra. Some of the units shown have capabilities not illustrated here, and details of the beam-processing package are given in Figs. 2 and 5. All scalers were actually located in the instrument area. Only the results from "Route 1" of analyzer No. 10 are reported here.

In the Slow Gating Circuit:

1. The pulse from the beam package is coincident (1 μsec) with a (B′C′) coincidence to give storage as a proton.

III. EXPERIMENTAL PROCEDURES

Available time did not allow thorough coverage of the periodic table or angle ranges. Table 3 shows the cases for which differential cross sections were measured. The choices made were intended to illuminate the variation in the differential cross section vs target mass number and scattering angle. Unfortunately the 10° data suffered from a large background and were dominated by elastic scattering, which disturbed a very large portion of the spectrum because of the broad spectrometer resolution.

Total flight paths were chosen as a compromise between counting rate and velocity resolution. All 10 and 30° data were obtained at 89 cm, while data at other angles were obtained at 69 cm. Detector C′ was placed in accordance with the demands made by the flight-time variations between counters B′ and C′, the need for all particles to traverse the slightly smaller counter C′, and the need at small scattering angles to keep detector C′ out of the beam. A shield thick enough to stop 160-MeV protons was positioned to protect the (B′C′) array from any particles in a wing of the beam.

Since energy loss in the target by the secondary particle was known to be a serious limitation, targets were placed with their normals as close as possible to the direction toward counter B′.

Target-out backgrounds were measured once for each series of runs at a given detector angle.

Listed below are the principal routine checks made to verify the operation of the spectrometer. Not included is the general checkout on assembly of the electronics. The list is approximately in order of decreasing frequency, ranging from once per run to once per day.

1. Relative counting rates of beam scalers were checked to assure reasonable consistency.
2. Timing checks at zero degrees verified the zero-time value. During most such checks two or three separate cable delays were employed to provide a check on the system conversion gain

Table 3. Target and Detector Configurations for Which Differential Cross Sections Were Obtained.

Target	10°	30°	45°	60°	90°	120°
Be		x				
C	x	x				
H_2O		x		x		
D_2O		x				
Aℓ	x	x	x	x	x	
Co	x	x	x	x	x	x
Bi	x	x				

(nsec/channel). These tests automatically checked the approximate telescope efficiency.

3. Bias checks were performed on the setting of the counting thresholds for the (B′C′) coincidence circuit, the time-to-amplitude converter, and the beam package thresholds.
4. The proton beam was aligned to the target holder and detector positioner, using Polaroid film.
5. Coincidence circuit resolving times were measured using the full-energy beam and variable delay lines.

Table 4 summarizes the estimated rms uncertainties of the various experimental parameters important to the data analysis, aside from the counting statistics. Where no range of values is indicated, the same estimates were appropriate for all runs.

IV. ANALYSIS FOR DIFFERENTIAL CROSS SECTION

Typical Raw Data

Figure 16 shows a typical experimental flight-time spectrum. The background was similarly small in most of the measurements for scattering angles of $> 30^{\circ}$. The solid curve approximates the available experimental resolution. The arrows indicate the sections of the curve corresponding to various secondary energies, illustrating that at the higher energies the information is contained in very few channels.

Background Analysis and Subtraction

Since at lower secondary-proton energies counts are spread over many channels because the resolution is broad from energy lost in the target, analyzer time channels were combined into bins. The width of each bin was made to depend on the uncertainty in the energy at birth of a proton giving rise to a pulse registered in that bin. The details of the binning process are not consequential, but the reader should realize that plotted points in the following cross section graphs do not correspond to equal flight-time intervals.

The nature of the proton detector is such as to imply that only the following backgrounds were important:

1. deuterons or other heavier secondary particles from the target,

Table 4. Estimated Standard Errors for Experimental Parameters Entering into Analysis of Proton Data

Beam energy	± 1.0 MeV[a]
Detector area	0.4%
Detector efficiency	1.5%
Slewing correction	0.25 of correction relative to 158 MeV
Time-to-amplitude conversion factor	1%
Zero of timing scale	0.1 to 0.25 nsec
Scattering angle	0.5°
Flight path on center line	0.3 cm
Lateral beam spot position	0.15 cm
Surface density of secondary proton telescope	1.5 mg/cm^2
Number of protons striking target	1 to 2%
Surface density of target	0.3 to 1.5% for metal targets; 3.5% for the water target
Angle of target normal	0.5°

[a]From measurements reported in R. T. Santoro et al., Space, Time and Energy Distributions of the Proton Beam of the Harvard University Synchrocyclotron, ORNL-3722 (January 1965).

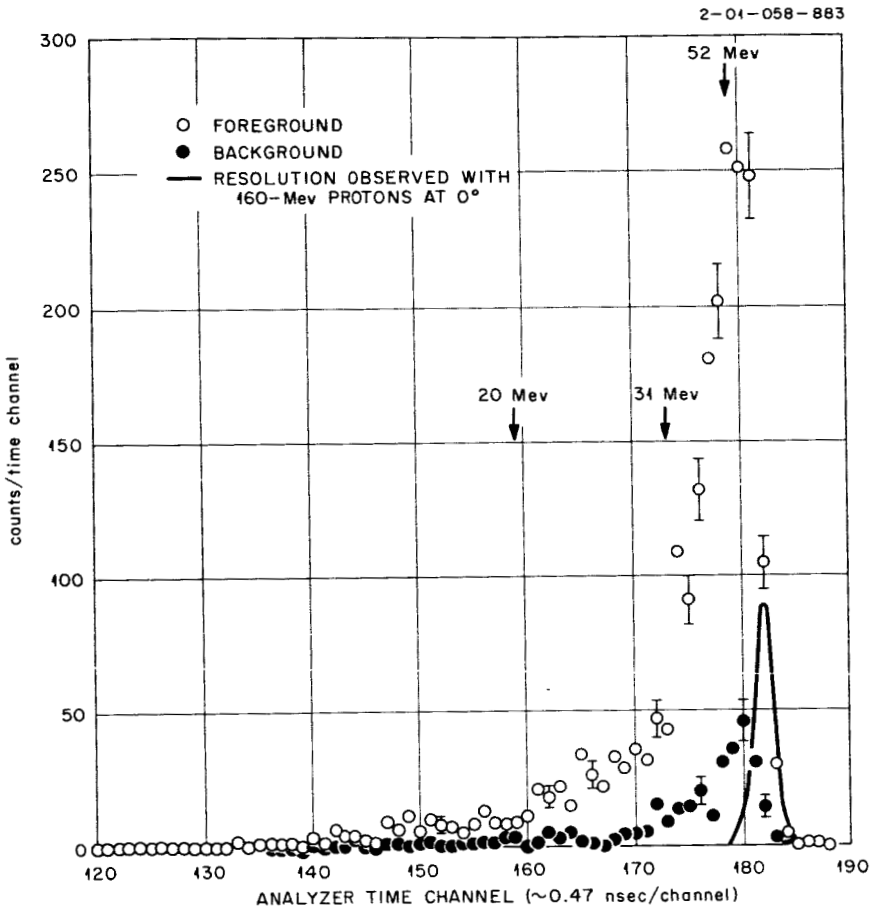

Fig. 16. Raw Pulse-Height Spectra from the Time-to-Pulse-Height Converter for Secondary Charged Particles from a 0.7-g/cm^2 Co Target, Along with the Corresponding Background.

2. beam protons scattered in the air volume near the target,

3. protons from the wings of the beam scattered in the target holder.

Since the volume of the target is small compared with the volume of air seen by the detector, since the cross section for interaction in the air is not much changed by the few MeV lost in the target, and since the detector singles rates were not much affected by the presence or absence of a target, the combined backgrounds 1 and 2 were determined by taking data in the standard manner with the target removed. The resulting background spectrum was normalized according to the relative numbers of accepted beam protons in the foreground and background runs and was subtracted on a channel-by-channel basis.

If the above analysis is correct, it should be possible to analyze the background to check the plausibility that it is caused entirely by air scattering. Table 5 summarizes the energy-integral cross-section information obtained by treating these background data on the assumptions that the proton beam was very concentrated, that detectors B′ and C′ had square rather than circular faces, and that only air scattering contributed. In computing the effective scattering volume of air, variations in detector solid angle were considered but the scattering cross section was assumed to be constant with angle over the detector face. The results are expressed as a ratio to $\sigma_{non}/4\pi$, where the nonelastic cross sections σ_{non} were taken as 0.23 barn for carbon, 0.27 barn for air, 0.44 barn for aluminum, and 0.73 barn for cobalt. At 30, 45, and 120° the results make the air-scattering hypothesis plausible, while at 10, 60, and 90° the number of background protons seems to have been two to six times too large. At 10° this is least surprising because part of beam counters A and A′ as well as the air volume could be seen by the secondary-proton telescope. At 60 and 90° the excess background presumably originated in the target holder. The target was supported at its edges, and the grazing angle between the target and the beam was smallest for the runs at 60°. The measured backgrounds were in no case a source of difficulty, since the relative background remained low (15%) even at 60°.

The wide variations in flight distances within the air-scattering volume prevented derivation of energy spectra from the background except at 90°, where there were too few counts for spectral analysis. One can

Table 5. Energy-Integral Relative Cross Sections, $\sigma_{p,xpy}(\theta)$, Derived for Air Scattering from Target-Out Background Data at 160 MeV, Compared with Results for Carbon, Aluminum, and Cobalt Targets.

	$4\pi\sigma(\theta)/\sigma_{non}$ [a]			
Scattering Angle[b] (deg)	Background (Air)	Carbon	Aluminum	Cobalt
10	45	18	22	25
30	4.0	3.4	3.0	2.7
45	2.6		2.3	2.2
60	6.9		1.2	1.2
90	0.62		0.33	0.37
120	0.23			0.17

[a] Values are normalized against the estimated nonelastic cross sections of Bertini, as given in the text.

[b] The angle between the beam axis and the line joining the centers of the target and the scattered proton detector.

observe in Fig. 16 that the background flight-time spectrum resembles the foreground one.

In this work elastic proton scattering is treated as a background because the experimental resolution is so poor that elastic scattering can spread counts over the entire part of the time spectrum corresponding to birth energies over 60 MeV. For the data obtained at 10° the apparent high-energy peak in the data was fitted by eye to the expected time distribution from elastic scattering, allowing estimation of the intensity of the elastic and near-elastic contribution. Table 6 compares observations made in this manner against anticipated elastic proton scattering based on optical-model estimations using parameters based on scattering experiments at 185 MeV. Agreement is moderate, depending on the uncertainty assigned the optical-model values. Some checks on the optical calculations are now available in the work of Roos[14] at 160 MeV, which unfortunately, however, are not for the same elements.

The experimental elastic and near-elastic cross sections listed in Table 6 were obtained by normalizing the expected time distribution of pulses from elastic scattering to the high-energy portions of the time spectra. (These contributions were then subtracted, including the appropriate low-energy tail, to give the segments of the nonelastic spectra displayed in Section V for a 10° scattering angle.) The theoretical estimates listed in Table 6 were obtained (G. Long, private communication, 1964), by averaging over the proton detector optical-model estimates[36] based on extrapolations of fits by Satchler and Haybron to the data of Johannson et al.[12] The near-elastic data from Bertini's intranuclear cascade results, discussed in Section VI, are believed to be somewhat high for the 0 to 14° interval.

Contributions from twofold scattering in the target were not carefully analyzed, but should amount to 1 to 3%.

Determination of the Differential Cross Sections

A local average value of the differential cross section $\sigma_{p,xpy}(\bar{E},\theta)$ can be computed corresponding to the contents C_k of the kth analyzer time-bin:

[36] R. Haybron, private communication. The parameters used were similar to those of G. R. Satchler and R. Haybron, Phys. Letter 11, 303-5 (1964), except the potential parameters were 5 to 15% greater in magnitude.

Table 6. Elastic and Near-Elastic Scattering at 10°

Target	Differential Cross Sections (mb/steradian)		
	From Experimental Elastic and Near-Elastic Scattering	From Intranuclear Cascade Near-Elastic Scattering (120-160 MeV)	From Averaged Optical-Model Elastic Scattering
C	300 ± 10[a]	60	240 ± 20[b]
Al	740 ± 25	87	740 ± 70[b]
Co	1500 ± 60	115	1900 ± 300[b]
Bi	4800 ± 200	150	5900 ± 1000[b]

[a]Uncertainties listed are those involved in the absolute cross section from the given run along with a 3% normalizing uncertainty. Counting statistical uncertainties are < 1%.

[b]These error estimates are based on uncertainties in the averaging process (3-10%) and on a comparison between the data of Roos (ref. 14) and the optical-model predictions which were employed (10-20%).

$$\bar{\sigma}_k = \frac{C_k}{\Delta_k \Delta\Omega P \nu \rho_k} \qquad (2)$$

where

$\bar{\sigma}_k$ = local average differential cross section corresponding to the counts C_k,

C_k = background-corrected number of counts in the kth time bin,

Δ_k = energy width of the kth bin,

$\Delta\Omega$ = detector solid angle subtended at the target,

P = number of protons penetrating the target during the accumulation of the C_k counts and satisfying the requirements of the circuit logic,

ν = number of target atoms per cm^2, viewed along the beam axis,

ρ_k = average efficiency of the telescope for protons over the solid angle range $\Delta\Omega$ and the energy range Δ_k.

The next section describes the estimation of Δ_k and of the energy E_k with which $\bar{\sigma}_k$ is associated. The solid angle of detector B′ is taken at its geometrical value on its face closest to the target, with corrections as discussed in Section II, "The Telescope for Secondary Protons." The number of useful protons in a run was the number adequately isolated from neighboring protons, about 0.7 of the total number of protons present. This number was generally obtained from the ISONPP scaler of Fig. 15, and an uncertainty was assigned on the basis of the degree of agreement among the various beam-package counting results, compared by taking into account counting losses through a fitted model of the beam time structure.[30] In the few cases for which this ISONPP scaler failed, the model allowed reasonably precise estimates of the number of counts it should have read.

Energy Calibration

A secondary proton from the target lost a variable amount of energy there and had to penetrate six successive material regions before entering detector B′ and losing enough energy in it to reach the detection threshold. The energy losses could have been determined by laborious hand calculation because most of the energy loss is in regions of high material density, whereas most of the flight time is spent in air.

Nonetheless, the relation between a proton's energy at birth and its flight time is sufficiently complex that a digital computer program was constructed to perform the computations with few calculational approximations.

The computation yielded the actual flight time of a secondary proton from various parts of the target, taking into account all the energy losses along the path, the statistical timing fluctuations or jitter, and the amplitude dependence of the time measurement or time slewing.

The detector system was analyzed in terms of a series of bin response functions $N_k(E)$, which give the probability that a proton born in the target at energy E and headed toward the detector's sensitive area would have been detected in the kth time bin. If protons of all energies were equally likely to be produced in the target, $N_k(E)$ would be the spectrum at birth of the protons which are registered in the kth bin. In this work $N_k(E)$ does not include the energy dependence of the spectrometer efficiency discussed in Section II and is normalized so that

$$\sum_k N_k(E) = 1 \text{ for } E > \text{EMIN} , \qquad (3)$$

where EMIN is the minimum energy of a proton required to be detected if it originated at a point in the target most distant from the detector.

The $N_k(E)$ functions give directly the energy resolution of the system, but the basic requirement is to obtain estimates of the observed cross sections. Such estimates could have been obtained by using a general data "unscrambling" scheme, but this was not done because of the nature of the predicted bin response functions and the large statistical uncertainties in the count data. Instead, the counts in a given bin were taken as representing an energy interval equal to the integral of $N_k(E)$, and the result was plotted at the mean energy of the bin response function. Details of this scheme are described after a discussion of the manner in which the $N_k(E)$ functions were calculated.

Energy Loss Calculations. -- Since the calculation of the $N_k(E)$ was repeated for each experimental run, required incremental energy-loss calculations over a series of materials, and involved averaging over a rather thick target, more than 10^6 evaluations of energy loss were

required. Since in the least favorable case 80% of a proton's energy was expended prior to its entry into the detector, reasonably precise calculations were necessary. With the exception of the relatively recent tables of Bichsel[37] and of Barkas and Berger,[38] available tabulations of energy loss of protons in various materials did not maintain good accuracy over the range of energies involved here (5 to 160 MeV); also, Bichsel's tables would have had to be extended to additional stopping materials. In response to these requirements the energy loss was computed from basic parameters for each case, according to a procedure described elsewhere[39] involving interpolation of "shell corrections" from a graph due to Turner.[40]

Calculation of the Response Functions. -- For a given proton energy E and target coordinate ξ, the flight time $t_f(E,\xi)$ to detection was computed by summing the flight times in a hundred or so flight-path increments. The time measured by the time spectrometer, t_m, is related to flight time by

$$t_m = t_d - t_f + \alpha(E,\xi) \ , \qquad (4)$$

where α is the time-slewing correction (given in Fig. 14) and is actually a function only of the proton energy at the face of detector B′; ξ is measured along the target-detector axis; the delay time t_d is a fixed quantity for a given experiment, its value being determined by rotating the detector into the proton beam and observing the time position of the resulting peak; and t_m is to be taken as a mean observed time. The actually observed time t_m' will fluctuate for each particle because of the (assumed) normally distributed timing fluctuations.

Each bin response function $N_k(E)$ is thus an integral over contributions from various parts of the target and over the time region within

---

[37] H. Bichsel, Sect. 8C in American Institute of Physics Handbook, 2nd ed., McGraw-Hill, New York, 1963.

[38] W. Barkas and M. Berger, Studies in Penetration of Charged Particles in Matter, NAS-NRC-1133.

[39] R. W. Peelle, Rapid Computation of Energy Losses, ORNL-TM-977 (1965).

[40] J. E. Turner, Ann. Rev. Nucl. Sci. 13, 1 (1963).

the kth bin. The assumption that reactions yielding secondary protons of energy E are equally likely at every depth in the target, even though the primary energy changes by 2 or 3 MeV, implies that to obtain the desired normalization of $N_k(E)$ the target integral should be a simple average:

$$N_k(E) = \int_{\text{Bin } K} dt'_m \int_{\text{Target}} \frac{d\xi}{\xi_o \sigma\sqrt{2\pi}} \exp\left\{-\frac{1}{2\sigma^2}\left[t'_m - t_m(E,\xi)\right]^2\right\} . \quad (5)$$

Here σ is the standard deviation of the statistical timing fluctuation and ξ_o is the thickness of the target along the ξ coordinate. The integrals (5) were performed numerically, using Gauss quadratures, for each of a series of energies E so chosen that integrals over E of the resulting $N_k(E)$ could be performed. Spacings in E varied from 4 MeV at 150 MeV to 1 MeV at 35 MeV and 0.1 MeV at 14 MeV. A three-point quadrature was used for the t_m integral for each 0.48-nsec time channel, and the results were simply summed into bins. This was adequate because the standard deviation σ of the jitter distribution was 0.43 nsec, and so the integrand did not change too rapidly. The most complex situation was presented by the ξ integral because for E low in the range the flight time changed more than 10 nsec for a given E from one surface of the target to the other. The problem was attacked by splitting the target automatically into different numbers of regions according to the proton energy considered, a nine-point Gaussian quadrature being used for each section of a target corresponding to a 2-nsec difference in flight time for a given energy at birth. The intervals were chosen so that the final results did not show significant sensitivity to the fineness of the integration mesh. Separate response functions were obtained for each run, since target energy losses changed for each case.

Figure 17 shows typical response functions computed for 70- and 90-cm flight paths, the latter being used for scattering at 30 and 10° where a greater number of high-energy particles were expected. Figure 18 shows a few sections through the response surface for constant E, which represent the spectra expected for monoenergetic protons. For plotting in Fig. 18, the computed intensity in each bin was divided by the bin width Δ_k.

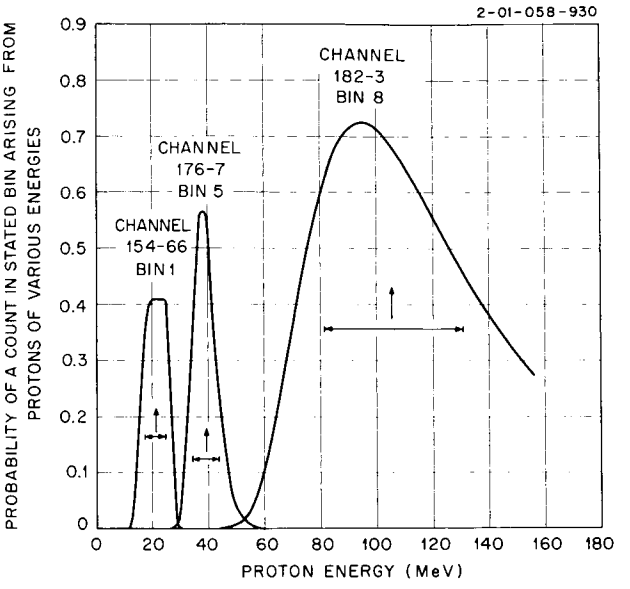

(a)

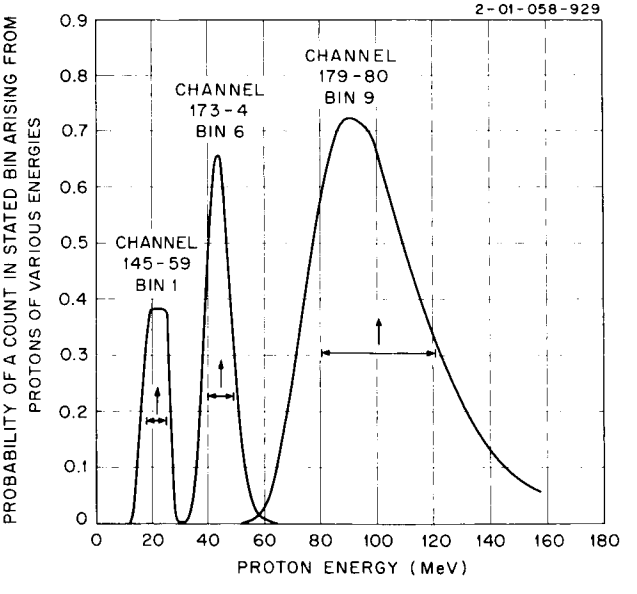

(b)

Fig. 17. Typical Birth Energy Distribution for the Flight-Time Spectrometer. (a) 70-cm flight path, (b) 90-cm flight path.

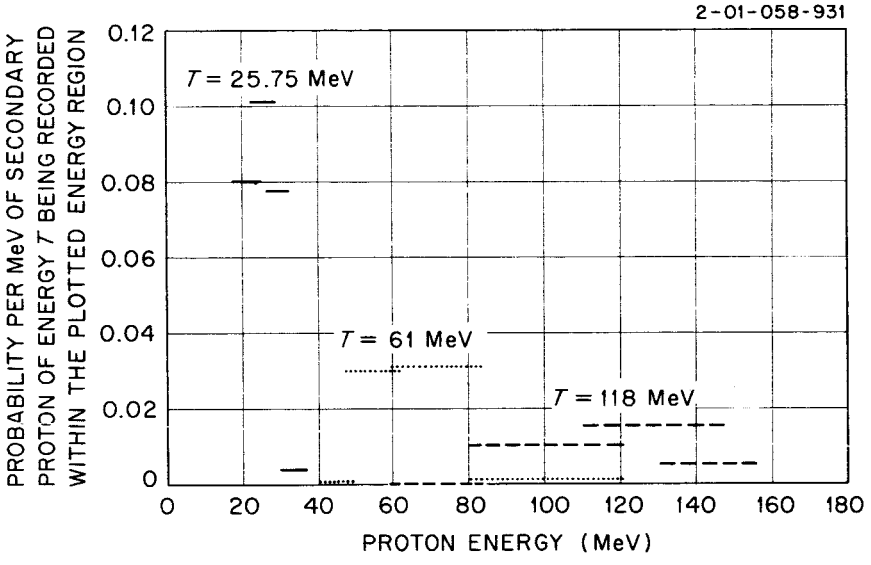

Fig. 18. Energy Resolution of Proton Flight-Time Spectrometer (90-cm Flight Path). Monoenergetic proton groups at the indicated energies are calculated to appear as shown.

Since the cross sections integrated over broad energy ranges are of interest, it is also important to understand the character of the response function for the sum of a number of bins or perhaps all bins. Typical integral response functions are shown in Fig. 19 for the 90-cm flight path.

The calculation of the response function ignored the effects of multiple scattering on the pathlength through the absorbing material, fluctuations in energy loss about the computed mean, the lateral size of the detector, the size of the beam spot on the target, and any suspected timing drifts during the course of a run. These approximations did not affect the results.

Interpretation and Application of the Response Functions. -- The cross-section data were analyzed using the following quantities obtained from the $N_k(E)$ by trapezoidal quadratures:

$$\Delta_k = \int_0^{E_{max}} N_k(E)\, dE \ ,$$

$$\bar{E}_k = \frac{1}{\Delta_k} \int_0^{E_{max}} E\, N_k(E)\, dE \ ,$$

$$V(E_k) = \left[\frac{1}{\Delta_k} \int_0^{E_{max}} E^2\, N_k(E)\, dE \right] - \bar{E}_k^2 \ , \qquad (6)$$

where E_{max} is the maximum energy kinematically possible for elastic scattering of the incident beam from the particular target. It is apparent from Fig. 17 that the effect of cutting off the integrals, Eq. (6), at E_{max} is very important for the highest energy bins. This procedure seems equivalent to inclusion of a priori information about the proton spectrum, and was useful because of the very great spread in the energies to which the highest bins were sensitive. In plots of the differential cross sections, data from each time bin are represented at $\bar{E}_k \pm \sqrt{V(E_k)}$ as in Fig. 18. Note that $\bar{E}_k$ is the average energy of the response function rather than of the energies of the particles actually detected. The assumption of correspondence is equivalent to the assumption at the outset of a flat spectrum over the energy regions of import, a proper

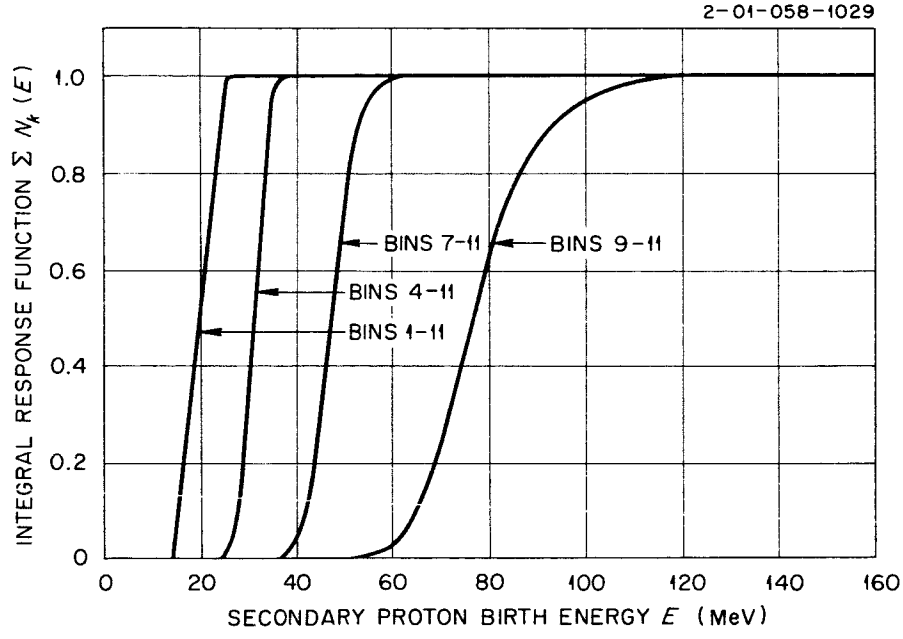

Fig. 19. Integral Response Function for Various Bin Combinations for a Typical 90-cm Flight-Path Case (30° Scattering from a Co Target).

assumption because there is a priori "insufficient reason" for a more complicated one. Such an assumption is commonplace for spectrometers with reasonably fine resolution. Of course, the experimental spectra are found to be a function of energy; so the a priori assumption is false.

In deducing the differential cross sections, Δ_k of Eq. (6) was employed as the energy width of the kth bin. This identification would be obvious if the $N_k(E)$ were shaped as rectangular blocks. The sum of the Δ_k over all bins is just the energy integral of the curve of Fig. 19, well identified with the total energy region studied. The differential cross section $\bar{\sigma}_k$ of Eq. (2) is the average differential cross section weighted by the response function $N_k(E)$:

$$\bar{\sigma}_k = \frac{1}{\Delta_k} \int_E \sigma(E)\, N_k(E)\, dE \ , \tag{7}$$

which is guaranteed the desired integral property by the unit normalization of $\sum_k N_k(E)$,

$$\sum_k \bar{\sigma}_k \Delta_k = \int_E \sigma(E)\, dE \sum_k N_k(E) \ . \tag{8}$$

Thus the integral cross section above the fuzzy low-energy cutoff of Fig. 19 may be obtained in the obvious fashion from the tabulated differential cross sections. The nearly linear low-energy cutoff in Fig. 19 is directly related to the thinning of the effective target at low energies where protons cannot penetrate the entire target and detector assembly. The energy width, the mean energy, and the energy variance of the bins used may be found in the data tabulations of the Appendix.

Two major difficulties of the employed analysis system were accepted: the bin response functions are not symmetrical, complicating the meaning of the presented data, and there is no provision for including available information from the pulse-height spectra in detector B′.

Propagation of Estimated Uncertainties

An attempt was made to perform a proper first-order estimate of uncertainties in the energies and the cross sections, using the

uncertainties of Table 4 and the counting statistical uncertainties. Contributions from seemingly independent variates were combined as the sums of squares, but where a given parameter entered into the result in two ways, the correlation was taken into account. For instance, the target thickness affects the number of scattering centers and also the size Δ_k of the energy bins through an effect on energy loss.

A first-order error analysis depends on generation of the partial derivatives of the result with respect to the uncertain experimental variates. In the case of the bin average energies E_k and the bin widths Δ_k this cannot be done trivially because there is no explicit expression relating the bin energies and widths to the experimental parameters via a flight-time computation. The required derivatives could have been obtained numerically by performing the entire calibration procedure with slightly altered input parameters, but it seemed (incorrectly!) that this would involve too high a computing cost. At the suggestion of R. L. Cowperthwaite the required derivatives were obtained with the help of a simplified energy-calibration analysis and the implicit function theorem.

In the simplified time-calibration model the time jitter distribution was ignored; so for a given birth position in the target the measured time was a unique function of birth energy. A series of secondary proton energies was chosen at the approximate divisions between adjacent energy bins, and the sensitivity of these energies to changes in the experimental parameters was studied, with all protons assumed to have originated at a single target position chosen to represent as well as possible the average over the target. A good choice proved impossible for the lowest and highest bins, but it was assumed that the simplified model could represent adequately the behavior of the energy uncertainties.

Tables 7 and 8 list the energy and uncertainty properties of a typical run with the 90-cm flight path, that for protons scattered from cobalt at 30°. Uncertainties on each cross section were separated according to whether or not they were "associated" with a particular point; if not, they had origin in uncertainties common to an entire energy spectrum, e.g., integrated beam strength or target thickness. In the tabulated data of the Appendix the statistical counting errors are broken out of the "associated" standard errors. When the cross sections are integrated

Table 7. Bin Energy Uncertainties[a] Arising from Various Experimental Uncertainties

Bin No.	Nominal Energy of Lower Edge	Energy Uncertainty (MeV)[b]: From Time per Channel on Analyzer (+ 0.005 nsec/ch)	From Time Zero (+ 0.3 ch)	From Beam Energy (+ 1 MeV)	From Timing Walk (+ 25% of walk correction)	From Flight Path Near Target (+ 0.04 cm)	From Flight Path Near Detector (+ 0.3 cm)	From Target Thickness (+ 6 mg/cm^2)	From Detector Thickness (+ 1 mg/cm^2)
1	19.2	- 0.05	0.04	0.00	0.11	0.00	0.02	0.04	0.01
2	23.8	- 0.14	0.18	0.00	- 0.01	0.01	0.05	0.06	0.01
3	27.6	- 0.18	0.29	0.04	- 0.22	0.01	0.06	0.05	0.01
4	31.1	- 0.21	0.40	0.04	- 0.46	0.02	0.07	0.05	0.00
5	35.9	- 0.24	0.58	0.07	- 0.89	0.02	0.09	0.05	0.00
6	40.6	- 0.29	0.87	0.07	- 1.60	0.03	0.12	0.05	0.00
7	48.2	- 0.38	1.42	0.15	- 2.35	0.05	0.15	0.07	0.01
8	60.7	- 0.46	2.33	0.22	- 3.10	0.07	0.19	0.07	0.01
9	81.8	- 0.51	4.05	0.41	- 3.68	0.10	0.20	0.06	0.01
10	115.7	- 0.26	4.95	0.48	- 2.15	0.10	0.11	0.03	0.00
11	140.6	~ 0	1.90	0.19	- 0.29	0.04	0.01	0.01	0.00

[a]The uncertainty breakdown is given for the positions of the nominal "edges" of the bins. To determine from this the uncertainties in a bin width from a given experimental uncertainty, one must subtract two successive numbers in a column.

[b]The energy standard errors shown are $(\partial E_i/\partial X_i)\,\Delta X_i$, where the quantities ΔX_i are the estimated uncertainties from Table 4 The most important contributions were from the time-slewing correction and the drift of the time-analyzer channel corresponding to zero time.

Table 8. Average Properties of Bins Listed in Table 7.

Bin No.	Mean Bin Energy (MeV)	Bin Width (MeV)	r.m.s. Energy Variation Within Bin (MeV)	Uncertainty in Energy Scale at Bin Edges (MeV)	Relative Bin Width Uncertainty[a] (%)	Relative Counting Uncertainty[a] (%)
1	21.5	4.3	3.5	0.24	5	13
2	25.7	3.7	3.1	0.41	6	14
3	29.4	3.4	3.0	0.65	8	12
4	33.5	4.6	3.1	1.1	10	13
5	38.2	4.3	3.4	1.9	16	18
6	44.5	7.3	4.6	2.8	12	11
7	54.4	11.8	7.1	3.9	10	9
8	71.1	19.3	11.9	5.5	9	6
9	100.4	35.0	20.1	5.4	5	6
10	129.0	38.8	18.3	1.9	14	7
11	142.7	5.7	12.2		16	24

[a]The combination of these two columns gives the "associated" uncertainty.

over energy only these counting uncertainties and the "nonassociated" errors remain important. The nonassociated or normalization uncertainties for the cross section of the run used for the example in Tables 7 and 8 amounted to 2.8%, combined from the following: 1.5% in beam strength, 1.6% in target surface density, 0.2% from target angle, 0.3% for detector area, 1.5% from spectrometer efficiency, and 0.7% from flight-path-length uncertainty.

V. RESULTS

Angle-Energy Differential Cross Sections for Protons on Nuclei

Numerical values of cross sections measured for secondary protons are tabulated in the Appendix, along with the necessary calibration information, and running sums of the tabulated values allow determination of the integrated cross sections $\sigma(\theta)$ over any desired energy range above the 20-MeV minimum energy. In this section are illustrations of the observed energy spectra. All tables and figures are given for the laboratory system.

Figure 20 illustrates the differential cross sections observed at 30° for various targets. In the plots the full length of each symbol along the energy axis is twice the standard deviation of the bin response function, and the symbol is centered at the mean bin energy. Two uncertainty values are shown on each cross section: the inner one, which is from counting statistical uncertainties alone, and the outer one, which includes the other error sources, particularly the uncertainty in the bin width. (This uncertainty often appears large, but recall that it does not imply an uncertainty in the number of protons detected. The uncertainties in the Δ_k are highly correlated among the various runs.) The plotted cross sections increase monotonically with atomic weight, and at the available resolution there is no apparent structure. However, the cross sections are less flat for the heavier nuclei, consistent perhaps with the interpretation that more complex interactions occur in the heavier target nuclei. Data from a water target imply that the cross section of oxygen is similarly shaped but that at 30° it is nearly as large as that for aluminum.

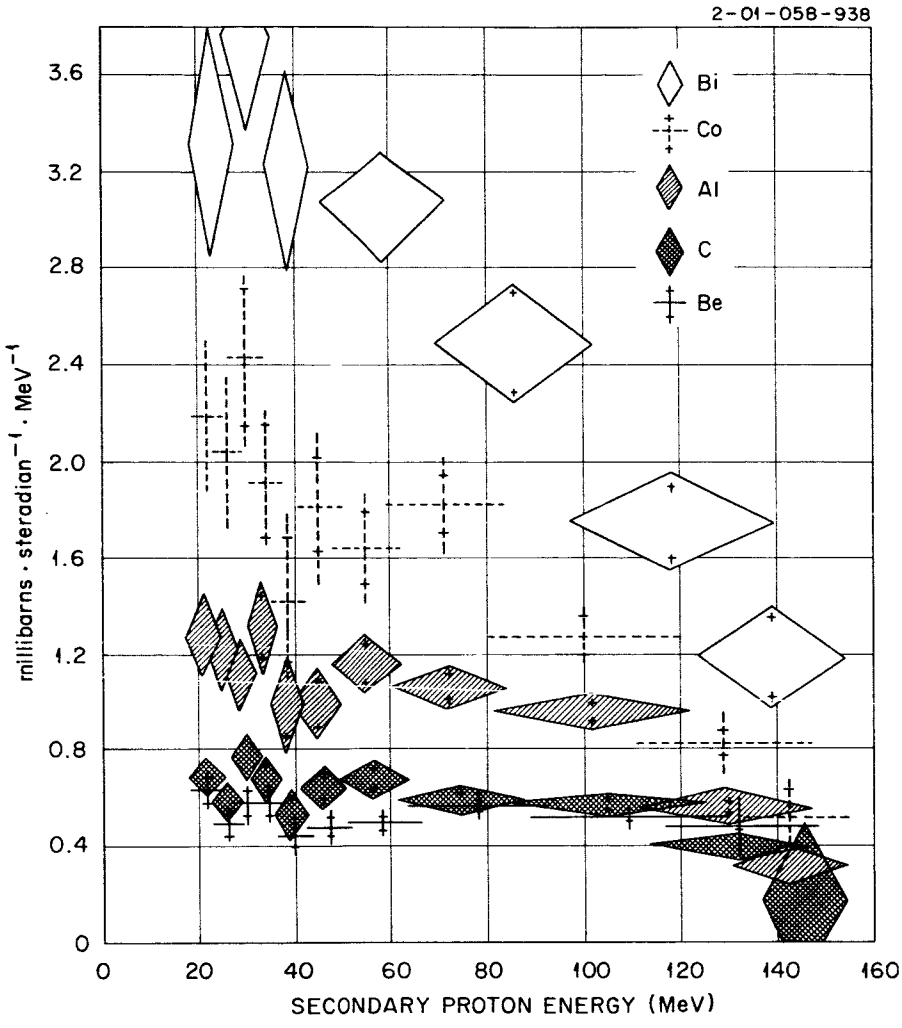

Fig. 20. Secondary-Proton Differential Cross Section at 30° for 160-MeV Protons on Various Elements.

At no other angle were enough data taken for a comparison similar to Fig. 20, but the sparse comparisons at larger angles are consistent with this relative behavior vs mass number. The data at 10^{o} were heavily influenced by elastic scattering down to rather low energies because of the skewed nature of the response functions and were subject to large counting backgrounds, but it was possible to obtain some results within the rather flat portion of the secondary proton spectrum between 20 and 60 MeV. Table 9 shows the averaged cross sections for the region between 20 and 60 MeV divided by $A^{2/3}$, which behaves like the nuclear area. Values are shown for observations at 10 and 30^{o} (from the data of Fig. 20). Note that at 10^{o} the observed cross section in this low-energy region is seen to increase with A less rapidly than does the nuclear area. This effect is not marked for secondaries at 30^{o}. Only the oxygen data appears to be anomalous at 30^{o}. The calculated values in Table 9 are from the cascade-plus-evaporation model as affected by detector resolution, described in Section VI, with uncertainties between 5 and 10%. Absolute cross sections for the 10^{o} data are given under the following section, "Integrals over the Energy Spectra."

Figures 21, 22, and 23 respectively illustrate the observed differential cross sections for carbon, aluminum, and cobalt at each angle measured. (The only distributions available for Bi and Be are in Fig. 20, and scattering from light and heavy water targets is illustrated in Figs. 24 and 25 in the next section, while data for Bi are given in the Appendix for 10^{o}.) The data at 10^{o} have had the elastic and nearly-elastic contribution subtracted rather arbitrarily, as indicated by the experimental cross sections listed in Table 6, and the plotted spectra are correspondingly terminated at the energy where the subtracted quantity becomes appreciable according to the calculated response functions. Figures 21-23 illustrate the "softening" of the secondary spectra as the angle is increased. Such a trend would be expected if the dominant reactions could be described as a short series of nucleon-nucleon encounters within the nucleus.

Scattering of Protons from Hydrogen in Water Targets

Figure 24 illustrates the scattering observed at 60^{o} from a water target, where the p-p scattering would be expected to appear at about 37 MeV. The data do show a prominent excess over what might be expected (see Section 6) from oxygen alone in an intranuclear cascade approximation.

Table 9. Averaged Cross Sections for 20- to 60-MeV Region at 10 and 30°, Divided by $A^{2/3}$

Element	$A^{2/3}$	Cross Sections (mb steradian^{-1} MeV^{-1}) x $A^{-2/3}$			
		θ = 10 deg		θ = 30 deg	
		Calc.	Exp.[a]	Calc.	Exp.[a]
Be	3.56			0.053	0.12
C	5.25	0.047	0.16	0.068	0.12
O (from H_2O and D_2O)	6.35			0.063	0.17
Aℓ	9.0	0.063	0.18	0.068	0.12
Co	15.2	0.064	0.13	0.065	0.12
Bi	35.0	0.037	0.08[b] ± 0.013	0.044	0.10

[a]Errors in the experimental values are about one in the last digit shown for the 10° data and half that big at 30°, where backgrounds were smaller.

[b]This uncertain value drops to 0.04 ± 0.013 if the energy region examined is terminated at 49 MeV instead of 62 MeV.

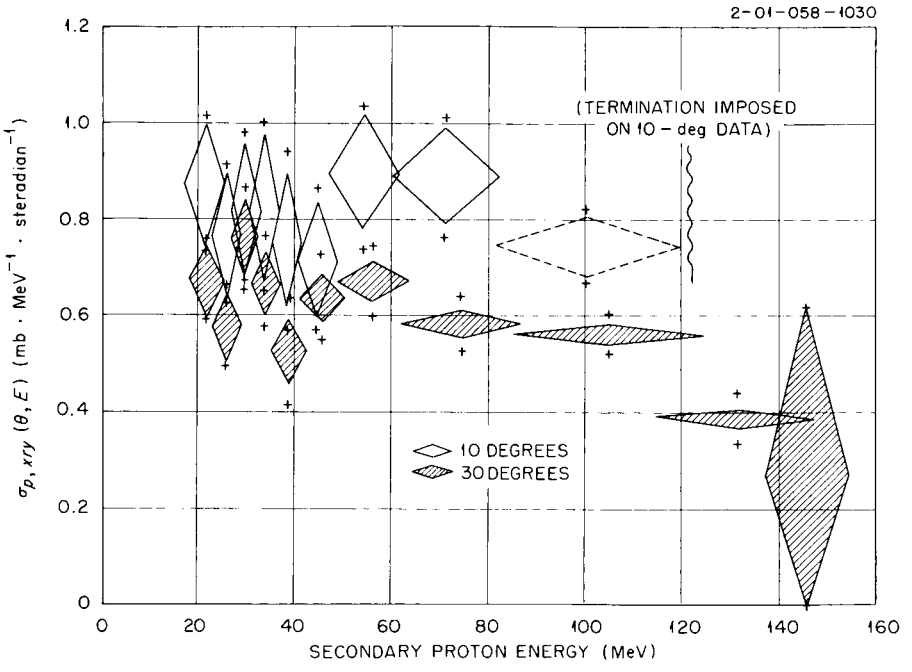

Fig. 21. Secondary-Proton Spectra from C at 10 and 30°. Beyond the indicated energy (~120 MeV), elastic scattering obscured the 10° data.

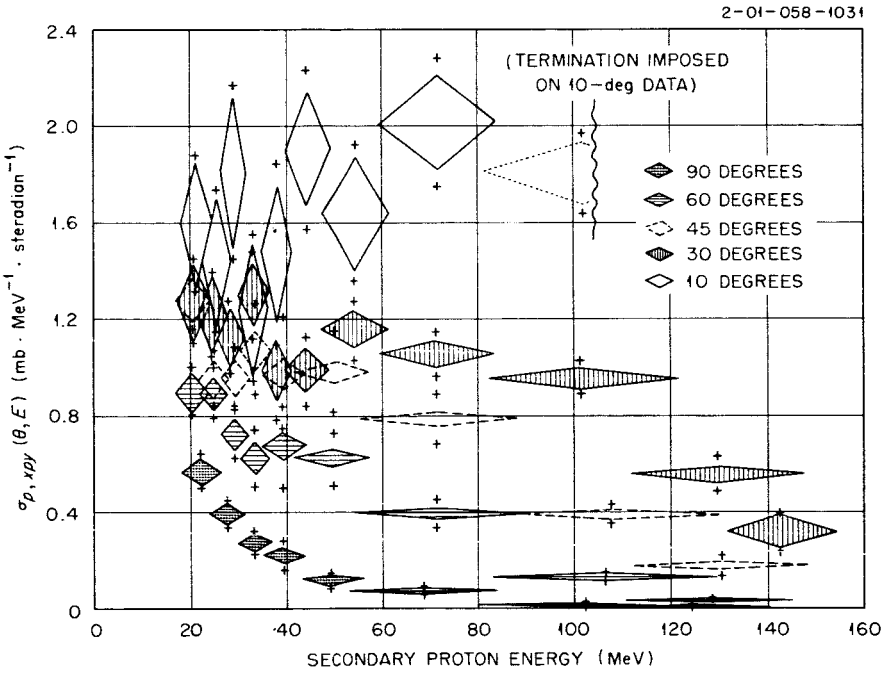

Fig. 22. Secondary-Proton Spectra from Aℓ at Various Angles. Beyond the indicated energy (~100 MeV), elastic scattering obscured the 10° data.

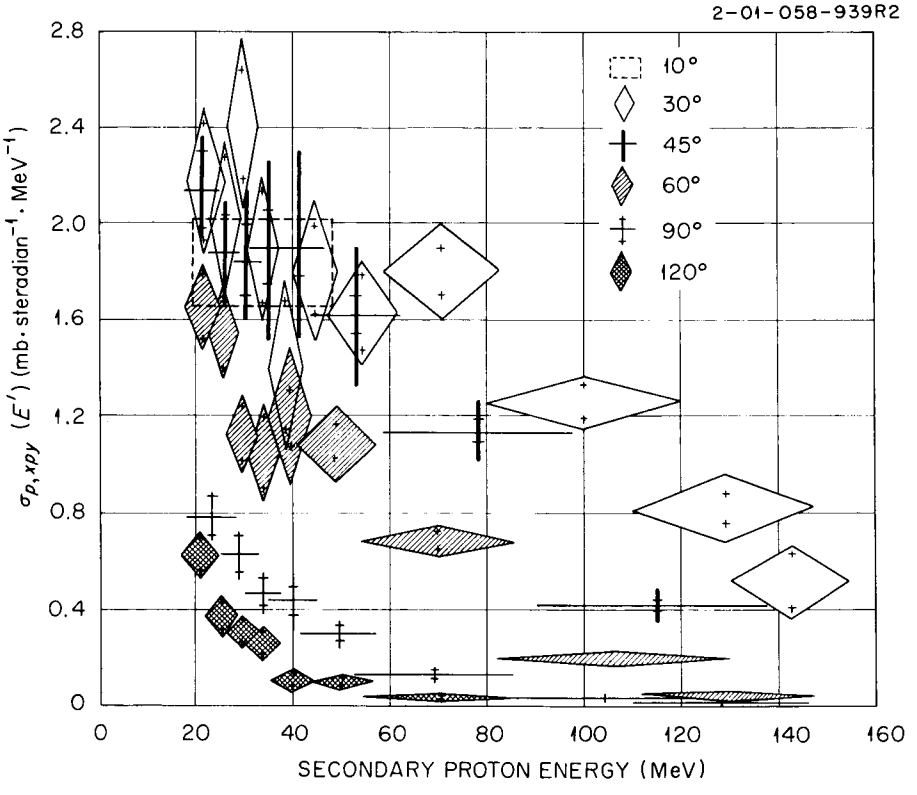

Fig. 23. Secondary-Proton Spectra from Co at Various Angles. The 10° data for energies above 50 MeV were obscured by elastic scattering.

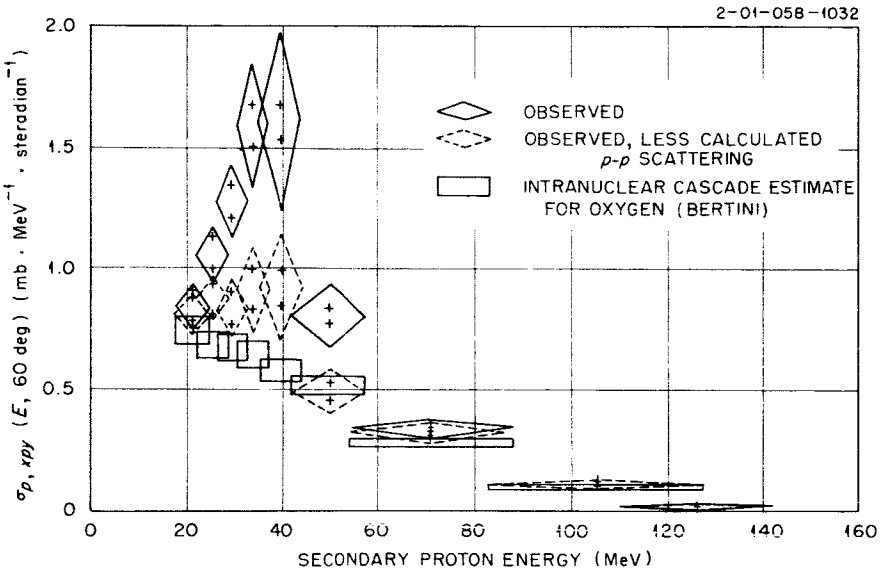

Fig. 24. 160-MeV Protons on H_2O; 60° Scattering. Oxygen cross sections are shown from Bertini's intranuclear cascade calculation and from a subtraction of estimated p-p scattering from the experimental data.

The comparison is complicated both by the energy resolution of the spectrometer and by the rapid variation of the scattered proton energy ($\sim E_o \cos^2\theta$) over the angular opening of the spectrometer. Thus the exhibited expected scattering from hydrogen is a broadened distribution. The position of the experimental peak appears correct, well within the assigned energy standard error at this energy of about 2 MeV. (This is the region of maximum pulse-amplitude correction to the timing signal.) The magnitude of the peak is also about correct if one takes the p-p center-of-mass differential cross section to be 3.7 ± 0.1 mb/steradian.[41] This conclusion is imprecise because the oxygen cross section was not measured and because the target thickness was poorly known, but it illustrates that the system was reasonably calibrated in energy and efficiency in the 40-MeV region, where disagreements with other results are significant. The predicted energy resolution is not sharply tested because of the energy broadening introduced by the rapid angular dependence of the scattered proton energy.

Scattering from a water target at 30° was also observed, but the energy resolution at the p-p scattering energy of 120 MeV is too coarse to allow a good separation of the effects of the hydrogen from those of the oxygen. The data for light- and heavy-water targets are shown in Fig. 25, along with an estimated oxygen cross section obtained by averaging the measured carbon and aluminum data of Fig. 20. In performing the average the magnitude of the cross section at any energy was assumed to vary as $A^{2/3}$, and the carbon data were given double weight though the two sets of data agreed within counting statistics after dividing by the approximate nuclear area. While this produces a spectral shape to aid in the inference of the effect of scattering from hydrogen, the oxygen cross section appears to be about 30% higher than expected at this angle, as shown for low energies by Table 9. In Fig. 25 the data from D_2O and H_2O agree reasonably well at the lower energies, considering the 5% uncertainty in each case in determining the target thickness. The hydrogen scattering is taken from the same center-of-mass value of 3.7 mb/steradian used at 60°, similarly smeared by the detector angle and energy resolutions. One can only say from the result that the apparent rise in the observed cross section at higher energies is about what would be

[41] W. Hess, Rev. Mod. Phys. 30, 368 (1958).

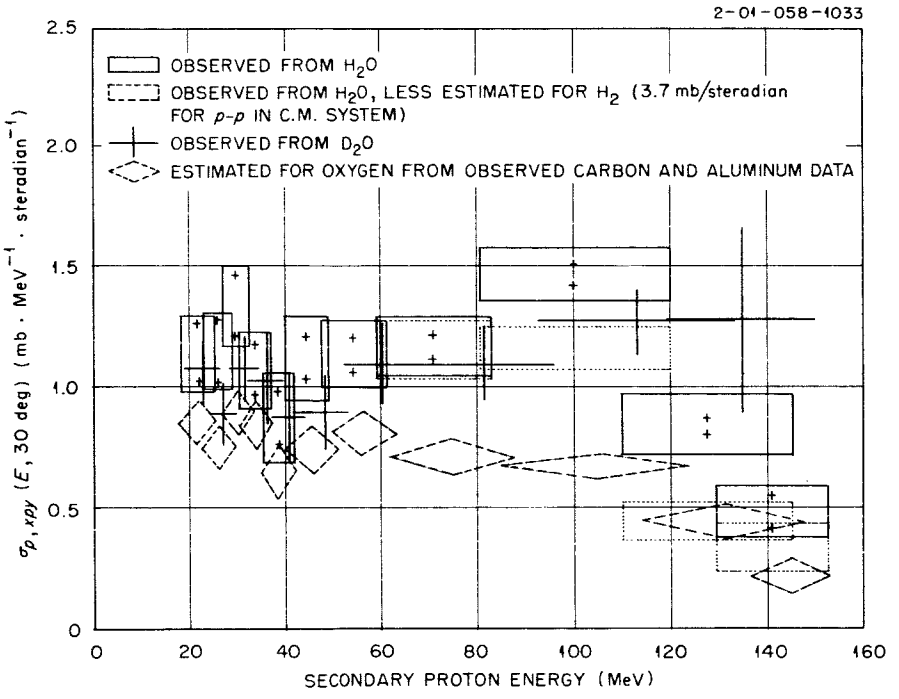

Fig. 25. Secondary Protons from H_2O and D_2O at 30°. Oxygen cross sections are shown estimated from C data and from the H_2O data less the estimated effect of p-p scattering.

expected from the hydrogen scattering. Scattering from deuterium is more complex; so detailed comparisons with the rather gross observed data were not considered worthwhile. Note that the hydrogen scattering should have no influence on the difference between interpolated and observed oxygen cross sections in the region below 70 MeV.

Integrals Over the Energy Spectra

Tables 10 and 11 give the integrals of the observed cross sections over the proton energy region above about 20 MeV as obtained by summing contributions from all the energy bins (except at 10°). Table 10 compares the experimental sums with computed ones, while Table 11 details the basis of the calculated estimates (discussed in Section 6). The calculated values take into account detector angular resolution. The integrated cross sections at 30° rise slightly more slowly than the nuclear area, consistent with Table 9 for the 20- to 60-MeV region, but this effect is not prominent in the few data at wider angles.

Figure 26 illustrates that the measured cross sections for aluminum and cobalt from Table 10 agree with each other remarkably well after they are divided by $A^{2/3}$. The hand-fitted curve of Fig. 26 was integrated to yield $\sigma(E > 20\ \text{MeV}) = 45A^{2/3}$ mb, or $\sigma(E > 20, A\ell) = 0.40$ barn, $\sigma(E > 30, \text{Co}) = 0.68$ barn. These values correspond to an averaged charged-secondary multiplicity of 1 proton per reaction for an effective nuclear radius of $1.2 \times 10^{-13}\ A^{1/3}$ cm. An analysis on this simplified basis should not be pressed.

Comparisons with Other Experiments

Very few other experiments have produced spectra which compare directly with those given here. Spectra observed at the 160-MeV energy at 60° by Gibson et al.[6] agree within their uncertainties for energies above 50 MeV, where both spectrometers operated, but there is rather general disagreement with the data of Roos,[14] who found markedly more intensity than we did at the high end of the spectra and a marked dip in the 40- to 50-MeV region even for rather wide angles. At energies in the 110-MeV region the Roos data fall well above the 60° spectra of Gibson for carbon and bismuth targets,[42] but Fig. 27 shows the only case where a nearly direct comparison of all three experiments is possible.

[42] W. Gibson, private communication, 1965; see ref. 6 for description of the Gibson experiment.

Table 10. Angle Differential Laboratory Cross Sections for Secondary Protons Above ~ 20 MeV Compared with Available Estimates.

Target	Angle (deg)	Energy Cutoff[a] (MeV)	$\sigma_{p,xpy}(\theta)$(mb/steradian) Estimated	Measured	$\sigma_{meas}A^{-2/3}$
Be	30	20.1	68 ± 1.5	70 ± 2	16.2
C	10[b]	20.0 to 59	9.7 ± 1.2	32.5 ± 2.3	
	30	19.9	90 ± 3	75 ± 3	14.3
Aℓ	10	19.6 to 59	23 ± 2	65 ± 4	
	30	19.5	133 ± 3	124 ± 4	13.8
	45	19.2	85.7 ± 1.6	80 ± 3	8.9
	60	19.2	45.0 ± 1.1	43 ± 1.5	4.8
	90	20.7	8.2 ± 0.4	11.4 ± 0.6	1.3
Co	10	19.9 to 61	39.7 ± 2.4	82 ± 7	
	30	20.0	196 ± 3	187 ± 7	12.3
	45	19.2	130 ± 2.3	128 ± 5	8.4
	60	19.3	67.5 ± 1.6	70 ± 3	4.6
	90	20.9	13.0 ± 0.6	21.2 ± 1.1	1.4
	120	19.7	3.35 ± 0.2	9.7 ± 0.7	0.64
Bi	10	18.6 to 62	57 ± 3[c]	126 ± 20[c]	
	30	18.7	269 ± 5	330 ± 14	9.5
H_2O	30	20.2	134 ± 3	152 ± 7	19.8[d]
	60	19.7	48 ± 1	54 ± 3	6.3[e]
D_2O	30	20.9	160 ± 6	157 ± 7	16.5[f]

[a]Taken for $\frac{1}{2}$ maximum sensitivity on a curve like that in Fig. 19 showing the integral response for all bins summed.

[b]All 10° data are integrated over the energy region indicated in the Energy Cutoff Column.

[c]As indicated in Table 9, estimated and measured values would agree here (± 30%) if the upper limit had been taken at 50 MeV.

[d]Based on an inferred oxygen contribution of 125 mb/steradian.

[e]Based on an inferred oxygen contribution of 40 mb/steradian.

[f]Based on an inferred oxygen contribution of 104 mb/steradian.

Table 11. Sources of Estimated Cross Sections

Target	Angle (deg)	Energy Cutoff (MeV)	σ(θ)(mb/steradian) Elastic[a]	Cascade[b]	Evaporation[c]
Be	30	20.1	3	64.3 ± 1.4	0.73 ± 0.03
C	10	20.0 to 59		9.2 ± 1.2	0.53 ± 0.04
	30	19.9	3	86.4 ± 2.3	0.54 ± 0.04
Aℓ	10	19.6 to 59		22.8 ± 1.5	0.67 ± 0.03
	30	19.5	7	125.2 ± 2.3	0.68 ± 0.03
	45	19.2	~ 0.5	84.4 ± 1.6	0.77 ± 0.03
	60	19.2	~ 0.04	44.2 ± 1.1	0.77 ± 0.03
	90	20.7	~ 0	7.6 ± 0.4	0.63 ± 0.03
Co	10	19.9 to 61		38.9 ± 2.4	0.82 ± 0.05
	30	20.0	7	188 ± 3	0.82 ± 0.05
	45	19.2	~ 0.5	128.2 ± 2.3	1.02 ± 0.05
	60	19.3	~ 0.05	66.5 ± 1.6	1.00 ± 0.06
	90	20.9	~ 0	12.2 ± 0.6	0.79 ± 0.05
	120	19.7	~ 0	2.38 ± 0.17	0.97 ± 0.06
Bi	10	18.6 to 62		55 ± 4	1.6 ± 0.1
	30	18.7	15	252 ± 5	1.5 ± 0.1
H_2O	30	20.2	5 + 26.6 ± ± 0.8[d]	101.8 ± 2	0.53 ± 0.02
	60	19.7	0.1 + 14.2 ± ± 0.4[d]	32.9 ± 0.9	0.62 ± 0.03
D_2O	30	20.9	5 + 53 ± 5[e]	101.5 ± 2	0.49 ± 0.02

[a] Uncertainties in the estimated elastic scattering are taken as 10% except in Co, O, and Bi, where they are 15 to 20% (see Table 6).

[b] The angular intervals generally used in sorting the Monte Carlo output were 0-14, 24-35, 40-50, 56-64, 85-95, and 110-131°. The "30°" interval for carbon was actually 21-38°. The uncertainties indicated arise from Monte Carlo statistics alone.

[c] The quoted uncertainties are of statistical origin. Fairly small changes in the evaporation model described in Section VI can produce up to 10% changes.

[d] The larger value is the estimated scattering from hydrogen assuming a center-of-mass differential cross section of (3.7 ± 0.1) mb/steradian. These values take into account averaging over the detector face as well as the relativistic transform to laboratory coordinates.

[e] This 53 mb/steradian estimate assumes that the integral cross section is the same as if the deuteron were unbound and that $\sigma_{n\text{-}p}(\theta)$ = (3.6 ± 0.6) mb/steradian in the center-of-mass-system [see Fig. 12 of A. F. Kuckes et al., Ann. Phys. (N. Y.) 15, 193 (1961) for experimental results at 146 MeV].

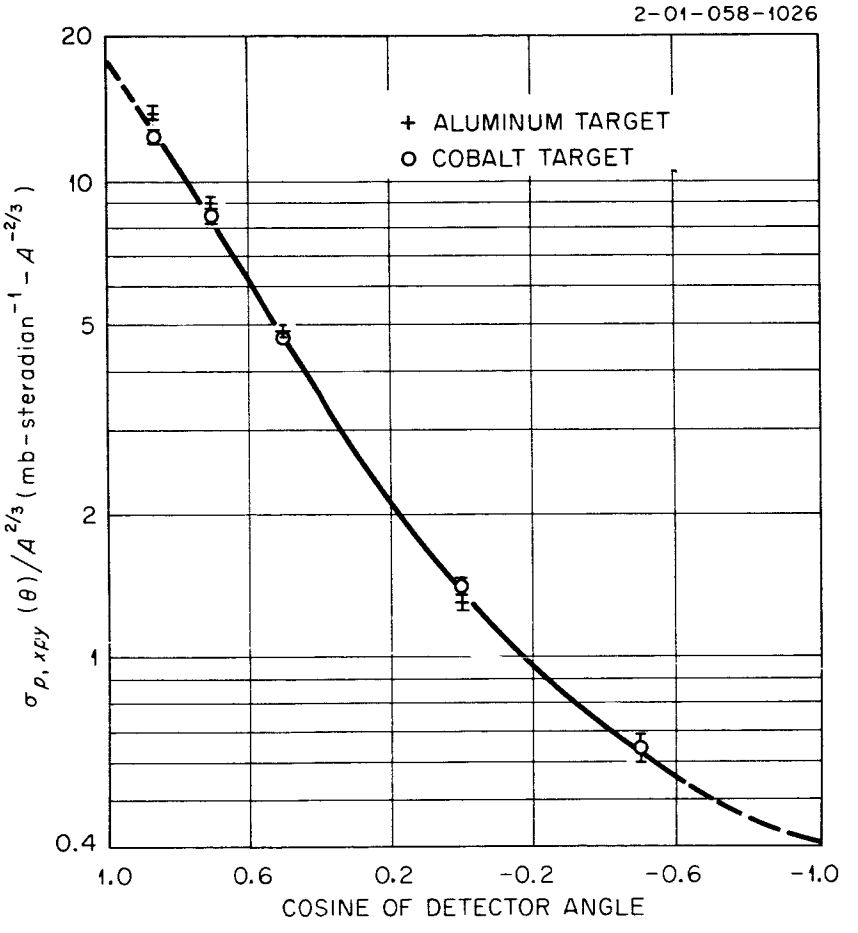

Fig. 26. Energy-Integrated Empirical Cross Sections per Nuclear Area for Aℓ and Co Targets.

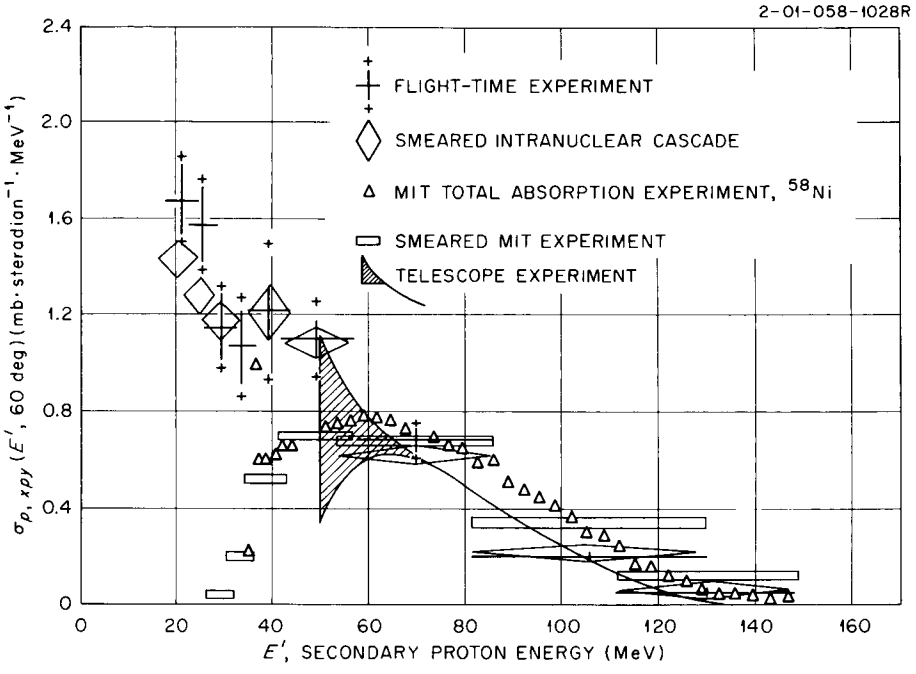

Fig. 27. Differential Cross Sections for 160-MeV Protons from Co at 60°. Data from this experiment are compared against those of Gibson, against intranuclear cascade estimates of Bertini discussed in Section VI, and against the experiment of Roos and Wall for Ni. The theoretical estimates have been smeared with the computed instrument response, and the MIT data are shown with and without such smearing.

The Roos data for ^{58}Ni is compared with cobalt data for the other experiments, which seems permissible because both Roos' work and the present experiment show a very small change in the observed spectra over the whole range from beryllium to bismuth. With or without inclusion of instrumental broadening, Roos' data lie definitely above the other experiments above 60 MeV and below this experiment at lower energies. Figure 28 shows a comparison at 30° for a carbon target which is typical of the observed discrepancies between Roos' data and ours for Be, Bi, and Ni vs Co. Roos' data are consistent with those of Fox and Ramsey,[10] though their energy regions do not overlap.*

As described in the introduction, experimental work at other energies may be examined for the general shape to be expected of the spectra at 160 MeV, but since the main interest in the experiment is just to observe the dependence on incident energy, not much appeal can be made here to this source of information.

VI. COMPARISON WITH THE INTRANUCLEAR CASCADE-PLUS-EVAPORATION MODEL

The Cascade-Plus-Evaporation Model

There is presently only one practical model for estimation of complete differential nucleon spectra from nonelastic reactions of 160-MeV primary protons. The method, often called the (intranuclear) cascade model, was introduced by Goldberger[43] and first extensively employed by Metropolis et al.[44] Monte Carlo techniques are used to follow the incident nucleon and its subsequent microscopic reaction products through a model nucleus which is a bundle of moving but noninteracting nucleons, with interaction cross sections used for collisions between the incident particle and any individual bound nucleon taken from free n-p and p-p scattering. "Nucleons" are followed along their classical paths in the three-dimensional

*There is no obvious flaw in the Roos experiment, which was carried out with much better energy resolution than the present one, allowing proper separation of elastic scattering. The linearity of their scintillator-phototube combination was not fully demonstrated, and the dip in the observed cross sections lies just above their spectrometer cutoff energy. Similarly, the experiment of Fox and Ramsey appears quite carefully done. The latter seem to have observed about a third of the "evaporation" yield seen by Bailey[11] at 190 MeV if targets having nearly equal atomic weights are compared.

[43] M. L. Goldberger, Phys. Rev. 74, 1269 (1948).

[44] N. Metropolis et al., Phys. Rev. 110, 185 and 204 (1958).

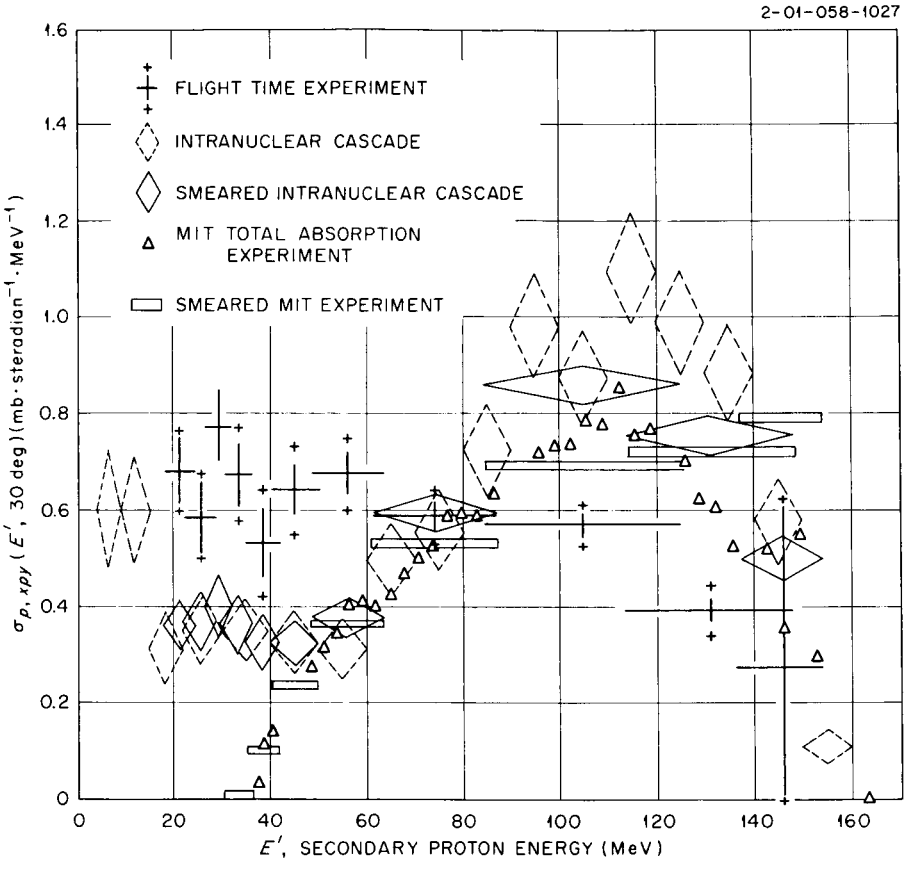

Fig. 28. Differential Cross Sections at 30° for Protons from 160-MeV Protons on C. Comparisons against the experiment of Roos and Wall and against the intranuclear cascade estimates of Bertini are exhibited with and without resolution smearing according to the calculated detector response functions.

model "nucleus" until they escape, fall below an arbitrary cutoff energy or one demanded by known binding energies, or have a collision with another nucleon, whose products in turn must be followed. The "target nucleon" momentum is chosen from the same distribution at every stage of the reaction. When no more particles can escape by this cascade process the "reaction" is terminated and the remaining excited nucleus can be treated by a nuclear evaporation (or other) model capable of dealing with redistribution of the available nuclear excitation energy to allow particle escape. Only one bound nucleon is assumed to be involved in each internal collision process, and neither neighboring nucleons nor the target as a whole shares in the energy-momentum conservation of a particular p-p or p-n collision. Thus secondary alpha particles or deuterons cannot be predicted by the cascade model in its pure form.

In applying the cascade model one generally assumes a spatial dependence of the average nuclear potential energy* and a momentum distribution for the bound target nucleons which is roughly appropriate to the nuclear size.

The cascade model depends for conceptual validity upon the idea of free flight for the incident nucleon over some distance within the nucleus, reinstituted by Serber[7] after a decade during which it seemed that a strong interaction model must always be used. This free flight requires apparent transparency of the nuclear material figured using free-particle cross sections or perhaps the smaller effective cross sections which take into account exclusion effects.[7,43]

Inspired by the classical kinematics employed within the nucleus, the additional assumption is usually stated that the incident nucleon wavelength be short enough for a single p-n or p-p interaction to be localized to the typical volume occupied by a bound nucleon, about 2×10^{-13} cm in diameter. In considering the relation of the intranuclear cascade model to the uncertainty relations, it helps to recognize that variables chosen at random need not be considered "sharp" even though the computer proceeds with machine precision. Thus the incident particle can have sharp momentum, and the minimum uncertainty in the collision

*Since the free-particle cross section is used, the nucleon being struck should not be thought to contribute to the average nuclear potential.

point is qualitatively related to the uncertainty in the scattered momentum, which has a range of possible values larger than the incident momentum itself. This broad uncertainty seemingly allows localization of a collision to a region of the same order as λ of the incident particle,* though only the approximate starting point for the scattered wave need be known to estimate the probability of an additional interaction. The usual assumption of a short incident wavelength is not a pressing requirement except in the very low energy region because the localization of the interaction point is produced by the collision and is not a prerequisite of it. If the localization uncertainty were a chief obstacle, it could be compensated in calculation by introducing a stochastically determined jump between the Monte Carlo collision point and the nominal starting point of the path of the scattered particle.

The most important conceptual validity requirements for the intranuclear cascade model are that a collision with any given nucleon be unlikely and that an impulse approximation hold, i.e., that the nucleus as a whole be unable to respond quickly enough to influence the course of a reaction. Even if the latter conditions are fulfilled, it would be remarkable if the whole high-energy part of the spectrum could be predicted by a nearly classical process which only considers reactions with one bound nucleon at a time.

The detailed comparisons in this report were prepared using the intranuclear cascade method and program of Bertini,[45] with his standard three-step set of nonuniform nuclear densities arranged to approximate the nuclear density distributions required by electron scattering data. With the nucleon densities for neutrons and protons fixed by the electron data within each of the three annular regions, a corresponding well depth was chosen such that degenerate noninteracting Fermi gases would have the proper density in each region if the least-bound particle had a separation energy of 7 MeV, independent of nuclide. In estimating the well depth required by the nucleon density, the correspondence principle

---

*A more quantitative statement is not known to have been worked out. λ is 10^{-13} cm for a 20-MeV proton. The standard uncertainty relation says that if the r.m.s. position uncertainty is λ the momentum r.m.s. uncertainty must be at least one half the momentum itself.

[45] H. Bertini, Phys. Rev. 131, 1801 (1963); also, Monte Carlo Calculations on Intranuclear Cascades, ORNL-3383 (1963).

(very large nucleus) approximation was made that the number of available states up to p_{max} in volume Ω is just proportional to Ωp^3_{max}. Thus the bound nucleons did not have momentum distributions corresponding to solutions of the wave equation in the assumed potential. The potential well in Bertini's model is used to obtain the local kinetic energy of a particle of given energy but is not used to provide any refraction of the incident or exit particles. The special assumptions of Bertini's model do not seem worse than those of the cascade model in general at the higher energies and for the heavier nuclei for which the model was intended; but in using the spectra down to 20-MeV outgoing energy, as we did, the neglect of refraction and of details of the intranuclear momentum distribution might be considered to be serious. Bertini's machine calculation produces a magnetic tape history which lists the parameters for all escaping particles from successive model encounters with the nucleus. These tapes were subsequently analyzed to give the estimated differential cross sections within particular angle and energy regions.

To account for the residual nuclear excitation, Bertini[45] employed an adaptation of the program EVAP written by Dresner[46] to carry out the methods of LeCouteur[47] and Dostrovsky[48] in a Monte Carlo evaluation of evaporation processes in which enough excitation energy is available to produce more than a single secondary nucleon. The evaporation theory is based upon the compound-nucleus hypothesis and through the reciprocity theorem upon equal a priori probability of decay of the compound nucleus into regions of phase space having equal volumes. The evaporation process continues until the estimated probabilities of decay via neutron, hydrogen, or helium isotopes are all null. The success of the program depends at least on its estimation of nuclear level densities, of barrier penetration factors, and of the masses of nuclei off the stability line.

---

[46] L. Dresner, EVAP, A Fortran Program for Calculating the Evaporation of Various Particles from Excited Compound Nuclei, ORNL-CF-61-12-30 (1961).

[47] K. J. LeCouteur, Chapt. VII in Nuclear Reactions, Vol. 1, Endt and Demeur, North Holland, Amsterdam, 1958.

[48] I. Dostrovsky et al., Phys. Rev. 116, 683 (1959) and 118, 781 and 791 (1960).

For use with the cascade analysis the original pre-evaporation nucleus and its excitation were determined from each particular cascade Monte Carlo history. The main conceptual difficulty in application of this equilibrium evaporation analysis to the postcascade nucleus is that the original "doorway" excitation does not inevitably lead to general heating of the nucleus but rather to spot heating. It has been suggested that decay of a system resulting from knockout of a tightly bound nucleon might more probably resemble an Auger effect, in which only two bound nucleons directly participate.

Fortunately, the de-excitation of the postcascade nucleus is not very important for the proton energy region > 20 MeV studied here; or at least the evaporation estimates determined here amount to but a small fraction of the predicted cross section except for the lowest energy bins and the widest detector angles.

The actual estimation of the cross sections was done using a program of Aebersold's, heavily influenced by the work of Schuttler,[49] which is a modification of the Bertini system designed to combine the sorting of the cascade results with the Monte Carlo evaporation estimation and the estimation of uncertainties in both. Aside from questions of data presentation, the Aebersold system differs in the following minor ways from that originally employed by Bertini:

1. A residual nucleus which is also a possible outgoing particle is counted as the latter, any nominal excitation energy being divided between particles. Nuclides such as ^{8}Be are allowed particle decay, even if the estimated decay probability is zero because of barrier effects. Unphysical multiple-evaporation paths in (Z,A) space for very light nuclides are avoided by prohibiting consideration of intermediate nuclei which are estimated to have a binding energy.

2. The channel energy is shared by the heavier fragment in the decay, and these energies are accumulated as if emission were at 90° in the center-of-mass system of the temporary nucleus. However, the initial momentum following the cascade process is ignored because inclusion leads to negative excitation energies for a few percent of the residual nuclei.

[49] R. Schuttler, Efficiency of Organic Scintillators for Fast Neutrons, ORNL-3888 (in press).

3. Additional masses are added to the tables of Wapstra[50] and Huizenga[51] used by Dresner, in the region below ^{27}Al, using recent experimental data as well as rough estimates and isobar relations. When the mass formula of Cameron [52] is used to supply unknown nuclear masses, it is asked to supply only the mass difference to a known nuclide of the same A. Approximate use of the Cameron relation for nuclei with Z or N < 11 was enabled by estimating values of "shell plus pairing" correction for Z and N up to 10. Because of the details of the Cameron system, the extensions make a change in some estimated masses as large as 20 MeV. Pairing corrections[53] to the effective excitation energy should also have been entered for the same light nuclides.

The above effects are of much significance only when the evaporation theory is applied to nuclei in the aluminum region or below, and one must suppose that there is little chance of the level density parameters used being valid for the light nuclides. Further, in this mass region all but the most basic assumptions of the intranuclear cascade are in trouble. The cascade-plus-evaporation method as used violates energy conservation at least by giving the postcascade excited nucleus no kinetic energy and by computing the initial excitation prior to the evaporation process on the basis of a fixed separation energy of 7 MeV for each nucleon liberated by the cascade (rather than using the actual nuclear mass later assumed in estimating the boil-off-decay of the same nucleus). In spite of these difficulties the cascade-plus-evaporation estimates are the best estimates available.

Another set of intranuclear cascade estimates has recently become available from Miller and his co-workers[54] at Columbia. Their model closely resembles Bertini's with two exceptions; their nuclear density functions have seven rather than three steps, and refraction and reflection at the potential steps may optionally be included. Preliminary comparison indicates that the predicted differential cross sections from

---

[50] A. M. Wapstra, Physica 21, 367 and 385 (1955).
[51] J. R. Huizenga, Physica 21, 410 (1955).
[52] A. G. W. Cameron, Can. J. Physics, 35, 1021 (1957).
[53] A. G. W. Cameron, Can. J. Physics, 36, 1040 (1958).
[54] J. Miller, private communication (1965).

the two calculations are similar, particularly when reflection and refraction are ignored. Inclusion of these effects into Miller's calculation for 160-MeV protons on cobalt tended to wash out the quasi-free scattering peak. Strengthening of the wide-angle scattering was also observed, by a factor of almost 3 at 120°. In the case of secondary protons from 160-MeV protons on bismuth at 30°, the Miller calculation gave no quasi-free peak and an integral cross section over energy which was only half as large as Bertini's; but for aluminum and cobalt targets no such large differences were apparent.

Folding-in of the Instrument Response

As in the comparisons with experiments having good energy resolution, all estimates from the Bertini cascade-plus-evaporation model were smeared with the computed spectrometer response functions $N_k(E)$ before comparisons were made. The plotted theoretical estimates are therefore less detailed than they might be, and they appear as if measured with the actual spectrometer except that elastic scattering is not included. In performing the smearing, the combined cascade and evaporation estimates were sorted into narrow bins which just match the energy ranges over which the computed response function was averaged for this purpose. The smearing operation was just a matrix multiplication in which the unit normalization of the response functions simplified the procedure. As can be seen from Figs. 27 - 29 the main effects of the smearing were that the evaporation contribution to the intensity in the lowest energy bin was greatly increased and the predicted quasi-free scattering peak in the spectrum for small angles was less sharp. In isolated cases each effect is illustrated below.

Comparison of the Integrated Cross Sections

Table 11 showed the estimated values of the nonelastic cross sections above the 20-MeV cutoff, as well as the evaporation proton contribution as computed by the Dresner routine. The methods used in estimating the elastic cross sections are outlined under "Background Analyses and Subtraction" in Section IV. When combined, the calculated values may be compared against experiment via Table 10.

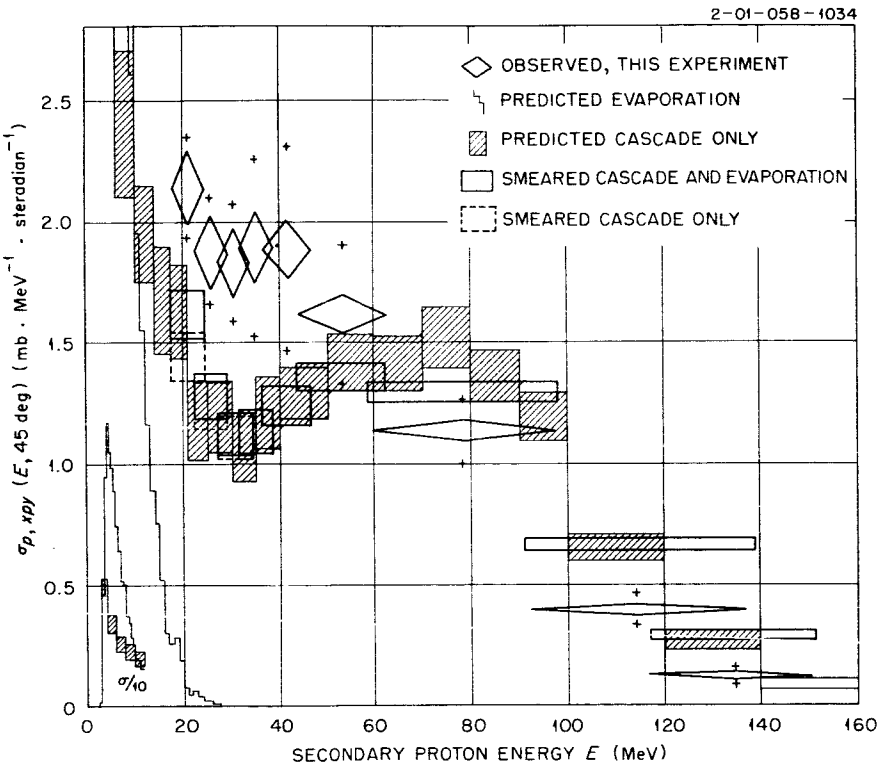

Fig. 29. Differential Cross Sections at 45° for Protons from 160-MeV Protons on Co. Experimental points are compared against the histogram representing the Bertini cascade and evaporation estimates and against the estimates as smeared by the detector resolution. The effect of the (assumed) isotropic evaporation contribution on the smeared spectrum is shown.

Agreement between measured and estimated values is least favorable for the 20- to 60-MeV integrated values at 10°, where for all but bismuth the measured values are twice as large as the estimated values.* The estimated values were also very seriously low for 90 and 120° from cobalt and aluminum. For scattering angles 30 through 60°, where the energy is split rather evenly in the initial encounter between incident and target nucleon, beryllium, aluminum, and cobalt targets show no disagreements. Bismuth and carbon targets at 30° show 20% discrepancies, and, if the method of estimating the deuterium contribution is valid, D_2O and H_2O give weakly inconsistent results. Estimation of the thickness of the water targets was quite difficult, and small amounts of water could have escaped between the experiment and the dimension measurements.

If the curve in Fig. 26 is accepted as a basis for determining the integral cross section for production of a charged particle having energy over 20 MeV by cobalt, a value of 0.68 barn is obtained, in disagreement with the corresponding Bertini cascade estimate of 0.56 barn. (Thirty percent of the area of Fig. 26 is for angles greater than 60°.)

Comparison of Differential Cross Sections

Figure 29 illustrates a typical comparison between calculation and observation, that for protons at 45° from a cobalt target, and clarifies the typical effect of inclusion of the evaporation estimate and of smearing the estimates to allow direct comparison with experiment. The observed spectrum is softer, showing no quasi-free scattering peak, though the area is the same. This contrast was slightly less marked for aluminum at 45°, but is strongly characteristic of all the comparisons at 30°, represented by Fig. 28. The difference is less pronounced for heavier nuclides, but the Bertini predictions at 30° for all nuclides show a broad peak near the energy which corresponds to that from quasi-free proton-nucleon scattering, whereas, as illustrated in Fig. 20, an unpeaked shape is characteristic of all the 30° experimental data of this report. Table 9 indicated the corollary strong disagreement in

*Table 9 indicated that this behavior persists for the low-energy portion of the 30° data.

the cross section observed for protons of less than 60 MeV. At these low energies the detector resolution does not influence the comparison.

Bertini reports[55] that the peaking near the maximum energy for small angles, clearly seen in comparisons with the Harwell data[19] at 140 MeV, is difficult to eliminate from the cascade estimates without destroying some of the fits to other data which were obtained from the model as originally presented. The peaking may be reduced by decreasing the size of the nucleus, whatever its shape. The more recent work of Miller[54] indicates that the peaking is reduced by reflection and/or refraction effects.

Figure 27 illustrated that for cobalt at 60° the cascade estimates are in excellent accord with the observed differential cross section. This was also observed for the aluminum target. The inferred oxygen cross sections of Figs. 24 and 25 indicate that the observations are considerably higher than expected, but note the unusually large uncertainty in the target thickness for those cases.

VII. CONCLUSIONS

The experimental results presented here seem consistent with those obtained by other investigators with the exception of the work of Roos and Wall.[14] Presumably the relatively low cross sections at high secondary energies could be explained if the resolution functions estimated here are too narrow, although most of the data on which to base the resolution estimates are for the 160-MeV region. The even stronger disagreement at 40 to 60 MeV is inexplicable; the approximately correctly observed p-p scattering strongly supports the results of this report since a hypothetical shape error in the spectra here would have to be associated with a considerable energy error in the position of the p-p peak in Fig. 24.

The comparisons with the cascade-plus-evaporation theory are remarkably encouraging, though the disagreements at 30° in the case of bismuth and carbon targets are puzzling. The general agreement of the angle and energy distributions is taken by us to imply the approximate

---

[55] H. Bertini, private communication (1964).

validity of the cascade model, at these energies, while no strong statement can be made about the evaporation contribution because it is so small. This remarkable general agreement disappears if one changes major features of the nuclear model such as the stepped edge, etc.[55]

There are two areas of consistent disagreement with the Bertini calculations:

1. Estimates at back angles are far too small. Single quasi-free interactions cannot give much backscattering, though such scattering in a real nucleus would be encouraged by a tendency to interact simultaneously with two nucleons -- or, put another way, by any failure of the notion that the target nucleons see only the fixed average potential. Further, the average excitation energy remaining with the nucleus after the cascade process is enough to aid the back-angle cross sections if the evaporation theory is badly in error, for instance, if levels near the ground state should have more than a priori equal probability of excitation in the decay of the compound system. States resulting from a single-knockout reaction appear indeed to be rather similar to states of low excitation. In any case, the exponential spectrum used by Dresner (modified by barrier effect) is only intended properly to represent the low-energy evaporated nucleons. (The series expansion performed to obtain the spectrum approximation is reasonably valid only for low-energy emitted particles.)

2. At angles through 45° the Bertini estimates give markedly less intensity than experiment at energies below 50 MeV or so, as well as quasi-free scattering peaks which are much more marked. These differences could arise from failures in the basic model assumptions or could represent the effect of neglected distortions produced by the average potential. The validity of the data in the 40-MeV region is supported by the results for the water target but is weakened by the failure of the experiment to differentiate between various secondary charged particles.

On the whole, this experiment encourages the interesting possibility that continuum cross sections may be predictable by some cascade model down to energies where the proton wavelength λ is about the size of a

target nucleon. From limited data the model seems as applicable to light nuclei as to medium-weight ones. These tentative findings could be illuminated by making studies at lower energies in both incident and secondary particles, by studying the back angles more carefully, by measuring at enough angles to allow reasonable integrals over solid angle, and by clearly identifying the particle type of all secondaries.

ACKNOWLEDGMENTS

The authors are grateful to A. M. Koehler for his friendly and full cooperation in helping us to understand the operation of the Harvard University Synchrocyclotron and to arrange for efficient use of the machine. We thank his entire crew for their aid during infrequent but puzzling difficulties. We are indebted to the Office of Naval Research for supporting the costs of our machine use.

Our performance of the experimental work on a rapid schedule depended upon extraordinary efforts by support groups at ORNL, particularly in detector and electronics design, fabrication, and testing, but also in other areas because of the particular difficulties of performing complex experiments far from the home laboratory. Accurate data collection depended upon careful and persistent help from O. W. Christian, F. Richardson, H. Weaver, C. O. McNew, R. Francis, C. Ball, and J. Madison.

Extensive help in analysis and computation was received from R. L. Cowperthwaite on the beam strength and duty factor, the detector time calibration, and especially the error analysis. P. M. Aebersold performed most of the history tape analyses that provided comparisons with the cascade-plus-evaporation theory, which H. Bertini most helpfully explained to us.

REFERENCES

[1]F. C. Maienschein, Neutron Phys. Div. Space Rad. Shielding Res. Ann. Progr. Rept. Aug. 31, 1962, ORNL CF-62-10-29, pp. 172-181.

[2]A. K. Strauch, Measurements of Secondary Spectra from High-Energy Nuclear Reactions, TID-7652, Book 2, p. 409 (1962).

[3]C. D. Zerby and H. Goldstein, Neutron Phys. Div. Ann. Progr. Rept. Aug. 1, 1963, ORNL-3499, Vol. II, pp. 63-66.

[4]R. W. Peelle et al., p. 331 in Second Symposium on Protection Against Radiations in Space, NASA SP-71 (1965).

[5]R. W. Peelle et al., Neutron Phys. Div. Ann. Progr. Rept. Aug. 1, 1963, ORNL-3499, Vol. II, p. 73.

[6]W. A. Gibson et al., p. 331 in Second Symposium on Protection Against Radiations in Space, NASA SP-71 (1965); W. R. Burrus, B. W. Rust, and C. Schneeberger, Neutron Phys. Div. Ann. Progr. Rept. Aug. 1, 1965, ORNL-3858, Vol. II, p. 82; W. Zobel, F. C. Maienschein, and R. Scroggs, Spectra of Gamma Rays Produced by the Interaction of 160 MeV Protons with Be, C, O, Al, Co, and Bi, ORNL-3506 (1965).

[7]Perhaps first suggested in the current context by R. Serber, Phys. Rev. 72, 114 (1947).

[8]P. C. Gugelot, p. 391 in Nuclear Reactions, Vol. I, P. M. Endt and M. Demeur, eds., North Holland Publishers, Amsterdam (1959-1962).

[9]C. E. Gross, The Absolute Yield of Low Energy Neutron from 190 MeV Proton Bombardment of Gold, Silver, Nickel, Aluminum, and Carbon, UCRL-3330 (1956).

[10]R. Fox and N. Ramsey, Phys. Rev. 125, 1609 (1962).

[11]L. E. Bailey, Angle and Energy Distribution of Charged Particles from High Energy Nuclear Bombardment of Various Elements, UCRL-3334 (1956).

[12]A. Johnson et al., Arkiv Fysik 19, 541 (1961).

[13]G. Gerstein, J. Niederer, and K. Strauch, Phys. Rev. 108, 427 (1957); A. E. Glassgold and P. F. Kellogg, Phys. Rev. 109, 1291 (1958).

[14]P. G. Roos, Elastic and Inelastic Scattering of High Energy Proton from Nuclei, Thesis, M.I.T. (1964). For elastic scattering, also see P. G. Roos and N. Wall, Phys. Rev. 140, 1237 (1965).

[15]J. B. Cladis, W. N. Hess, and B. J. Moyer, Phys. Rev. 87, 425 (1952).

[16]L. S. Azhgirey et al., Nucl. Phys. 13, 258-280 (1958).

[17]T. C. Randle et al., Phil. Mag. 44, 425 (1953).

[18]B. K. Nelson, G. Guernsey, and B. Mott, Phys. Rev. 88, 1 (1952).

[19]P. H. Bowen et al., Nucl. Phys. 30, 475 (1962).

[20]G. M. Temmer, Phys. Rev. 83, 1067 (1951).

[21]A. K. Strauch and F. Titus, Phys. Rev. 103, 300 (1956) and, 104, 191 (1956).

[22]J. A. Hofmann and A. K. Strauch, Phys. Rev. 90, 449 (1953).

[23]J. P. Garron et al., J. Phys. Radium 21, 322 (1960).

[24]J. Genin et al., J. Phys. Radium 22, 615 (1961).

[25]P. Radvanyi and J. Genin, J. Phys. Radium 21, 322 (1960).

[26]J. Hadley and H. York, Phys. Rev. 80, 345 (1950).

[27]P. F. Cooper, Jr., and R. Wilson, Nucl. Phys. 15, 373 (1960).

[28]W. N. Hess and B. J. Moyer, Phys. Rev. 101, 337 (1956).

[29]R. T. Santoro et al., Space, Time, and Energy Distribution of the Proton from the Harvard University Synchrocyclotron, ORNL-3722 (Jan. 1965).

[30]R. T. Santoro and R. W. Peelle, Measurement of the Intensity of a Proton Beam of the Harvard University Synchrocyclotron for Energy-Spectral Measurements of Nuclear Secondaries, ORNL-3505 p. 38 (March 1964).

[31]N. W. Hill et al., Performance Characteristics of Modular Nanosecond Circuitry Employing Tunnel Diodes, ORNL-3687 (1964).

[32]K. R. Symons, Fluctuations in Energy Lost by High Energy Charged Particles in Passing Through Matter, Thesis, Harvard University (1948).

[33]R. W. Peelle, Nucl. Instr. Methods 29, 293-298 (1964).

[34]H. C. Evans and R. H. Bellamy, Proc. Phys. Soc. 74, 483 (1959).

[35]T. A. Love et al., Absolute Efficiency Measurements of NE-213 Organic Phosphors for the Detection of 14.4 and 2.6 MeV Neutrons, ORNL-3893 (in preparation).

[36]R. Haybron, private communication. The parameters used were similar to those of G. R. Satchler and R. Haybron, Phys. Letter 11, 303-5 (1964), except the potential parameters were 5 to 15% greater in magnitude.

[37]H. Bichsel, Sect. 8C in American Institute of Physics Handbook, 2nd ed., McGraw-Hill, New York, 1963.

[38]W. Barkas and M. Berger, Studies in Penetration of Charged Particles in Matter, NAS-NRC-113.

[39]R. W. Peelle, Rapid Computation of Energy Losses, ORNL-TM-977 (1965).

[40]J. E. Turner, Ann. Rev. Nucl. Sci. 13, 1 (1963).

[41]W. Hess, Rev. Mod. Phys. 30, 368 (1958).

[42]W. Gibson, private communication, 1965; see ref. 6 for description of the Gibson experiment.

[43]M. L. Goldberger, Phys. Rev. 74, 1269 (1948).

[44]N. Metropolis et al., Phys. Rev. 110, 185 and 204 (1958).

[45]H. Bertini, Phys. Rev. 131, 1801 (1963); also, Monte Carlo Calculations on Intranuclear Cascades, ORNL-3383 (1963).

[46]L. Dresner, EVAP, A Fortran Program for Calculating the Evaporation of Various Particles from Excited Compound Nuclei, ORNL-CR-61-12-30 (1961).

[47]K. J. LeCouteur, Chapt. VII in Nuclear Reactions, Vol. 1, P. M. Endt and M. Demeur, North Holland, Amsterdam, 1958.

[48]I. Dostrovsky et al., Phys. Rev. 116, 683 (1959) and 118, 781 and 791 (1960).

[49]R. Schuttler, Efficiency of Organic Scintillators for Fast Neutrons, ORNL-3888 (in press).

[50]A. M. Wapstra, Physica 21, 367 and 385 (1955).

[51]J. R. Huizenga, Physica 21, 410 (1955).

[52]A. G. W. Cameron, Can. J. Physics, 35, 1021 (1957).

[53]A. G. W. Cameron, Can. J. Physics, 36, 1040 (1958).

[54]J. Miller, private communication (1965).

[55]H. Bertini, private communication (1964).

APPENDIX: Tables of Measured Cross Sections

The tables below give bin properties, experimental cross sections, and relative errors, all in the laboratory coordinate system. The format includes the laboratory angle θ in degrees, the target thickness along the target-detector axis, and the relative nonassociated standard error for each run. The total combined, associated (assoc), and count standard errors are relative to unity. The data are arranged by scattering angle in order of increasing atomic weight. At 10° the data obtained by subtracting a fitted elastic and near-elastic contribution are given in brackets adjacent to the unretouched values. The data are questionable in the regions so marked. Where no values are given in the parentheses, the uncertainty was prohibitive.

E_k (MeV)	Δ_k (MeV)	$\sqrt{V_k(E)}$ (MeV)	$\sigma(\theta,E_k)$ (mb MeV^{-1} steradian^{-1})	Relative Errors Combined	Assoc	Count
	$\theta = 10^{\circ}$ from 0.50-g/cm^2 C, $(\frac{\delta\sigma}{\sigma})_{na} = 2.3\%$					(Index 12058)
21.4 ± 0.2	4.1	3.5	0.89	0.16	0.16	0.15
25.5 ± 0.3	3.7	3.1	0.78	0.19	0.19	0.18
29.1 ± 0.5	3.3	2.9	0.83	0.21	0.21	0.19
33.2 ± 0.8	4.6	3.0	0.83	0.20	0.20	0.18
38.0 ± 1.5	4.3	3.3	0.77	0.25	0.25	0.19
44.2 ± 2.3	7.3	4.6	0.73	0.20	0.20	0.16
54.2 ± 3.3	12.0	7.1	0.91	0.16	0.16	0.13
71.0 ± 4.7	19.3	11.9	0.90(0.90)	0.14(0.14)	0.14	0.11
100.4 ± 5.5	35.2	20.3	1.25(0.75)	0.07(0.10)	0.07	0.05
129.4 ± 3.7	39.6	18.6	5.0 (...)	0.15(...)	0.14	0.02
143.3 ± 0.9	6.0	12.4	14.7 (...)	0.18(...)	0.18	0.02
	$\theta = 10^{\circ}$ from 0.55-g/cm^2 Aℓ, $(\frac{\delta\sigma}{\sigma})_{na} = 2.4\%$					(Index 12070)
21.1 ± 0.2	4.3	3.3	1.6	0.18	0.17	0.17
25.3 ± 0.3	3.8	2.9	1.5	0.20	0.20	0.19
29.0 ± 0.5	3.4	2.8	1.8	0.20	0.20	0.18
33.2 ± 0.9	4.7	2.9	1.2	0.25	0.25	0.23
38.0 ± 1.5	4.4	3.3	1.5	0.25	0.25	0.19
44.5 ± 2.3	7.6	4.7	1.9	0.18	0.17	0.13
54.7 ● 3.4	12.1	7.3	1.7	0.17	0.17	0.15
72.0 ± 4.8	19.9	12.3	2.0(2.0)	0.13(0.13)	0.13	0.10
102.0 ± 5.5	36.2	20.6	3.2(1.8)	0.07(0.09)	0.07	0.04
130.4 ± 3.9	38.3	18.3	13.2(...)	0.15(...)	0.15	0.01
143.8 ± 0.9	5.0	12.2	36.8(...)	0.16(...)	0.16	0.02

Tables of Measured Cross Sections - cont.

E_k (MeV)	Δ_k (MeV)	$\sqrt{V_k(E)}$ (MeV)	$\sigma(\theta,E_k)$ (mb MeV^{-1} steradian^{-1})	Relative Errors Combined	Assoc	Count
	θ = 10° from 0.70-g/cm² Co, $(\frac{\delta\sigma}{\sigma})_{na}$ = 2.5%					(Index 12090)
21.5 ± 0.2	4.3	3.4	2.4	0.20	0.20	0.19
25.7 ± 0.3	3.8	3.1	1.6	0.30	0.30	0.29
29.4 ± 0.5	3.4	2.9	2.3	0.25	0.25	0.23
33.6 ± 0.9	4.8	3.1	1.4	0.36	0.36	0.35
38.6 ± 1.5	4.5	3.4	1.7	0.32	0.32	0.28
45.1 ± 2.4	7.8	4.8	1.8	0.25	0.25	0.22
55.6 ● 3.5	12.4	7.4	2.5	0.19	0.19	0.16
73.3 ± 4.8	20.4	12.7	3.3(3.3)	0.13(0.13)	0.13	0.10
103.9 ± 5.4	37.2	20.8	6.6(3.1)	0.07(0.10)	0.06	0.03
131.4 ± 3.5	36.6	17.9	28.5(...)	0.15(...)	0.15	0.01
144.2 ± 0.9	4.2	11.9	77.7(...)	0.15(...)	0.15	0.02
	θ = 10° from 0.87-g/cm² Bi, $(\frac{\delta\sigma}{\sigma})_{na}$ = 2.3%					(Index 12102)
20.0 ± 0.3	3.6	2.9	2.1	0.59	0.59	0.59
23.5 ± 0.3	3.3	2.7	2.1	0.60	0.60	0.60
26.7 ± 0.4	3.0	2.5	1.3	1.03	1.03	1.03
30.3 ± 0.8	4.0	2.7	1.4	0.97	0.97	0.97
34.1 ± 1.0	3.5 γ	2.7	-1.1	1.31	1.31	1.31
38.6 ± 1.7	4.7	3.4	3.1	0.43	0.42	0.39
45.4 ± 2.6	8.3	5.0	1.5	0.66	0.66	0.65
56.6 ± 3.6	13.1	7.8	6.1	0.20	0.20	0.18
75.4 ± 5.0	21.7	13.5	12.3(12.2)	0.11(0.11)	0.11	0.08
107.2 ± 5.3	39.3	21.1	28.6(13.0)	0.07(0.08)	0.06	0.02
134.0 ± 3.2	36.0	17.3	114.0(...)	0.13(...)	0.13	0.01
148.6 ± 0.8	0.2	8.7	494.0(...)	0.17(...)	0.17	0.07
	θ = 30° from 0.55-g/cm² Be, $(\frac{\delta\sigma}{\sigma})_{na}$ = 2.1%					(Index 12038)
21.7 ± 0.2	4.5	3.5	0.64	0.10	0.10	0.09
26.1 ± 0.4	3.9	3.1	0.50	0.13	0.13	0.11
30.0 ± 0.7	3.6	2.9	0.58	0.13	0.13	0.09
34.3 ± 1.1	4.9	3.1	0.58	0.14	0.14	0.08
39.7 ± 1.9	4.9	3.6	0.45	0.21	0.21	0.11
46.7 ± 2.9	8.6	5.2	0.48	0.14	0.14	0.07
58.4 ± 4.2	13.6	8.1	0.50	0.13	0.13	0.06
78.2 ± 6.0	22.9	14.3	0.57	0.11	0.11	0.04
109.6 ± 6.2	40.0	20.0	0.52	0.08	0.08	0.03
132.3 ± 2.6	27.3	15.5	0.49	0.24	0.240	0.04

Tables of Measured Cross Sections - cont.

E_k (MeV)	Δ_k (MeV)	$\sqrt{V_k(E)}$ (MeV)	$\sigma(\theta,E_k)$ (mb MeV^{-1} steradian^{-1})	Relative Errors Combined	Assoc	Count
θ = 30° from 0.50-g/cm² C, $(\frac{\delta\sigma}{\sigma})_{na}$ = 2.3%						(Index 12026)
21.5 ± 0.2	4.4	3.5	0.68	0.12	0.12	0.11
25.8 ± 0.4	3.8	3.1	0.59	0.14	0.14	0.13
29.5 ± 0.5	3.4	2.9	0.77	0.13γ	0.13	0.10
33.8 ± 0.9	4.8	3.0	0.67	0.14	0.14	0.10
38.8 ± 2.4	4.6	3.5	0.53	0.21	0.21	0.13
45.4 ± 2.5	8.0	4.9	0.64	0.14	0.14	0.08
56.2 ± 3.5	12.7	7.6	0.68	0.11	0.11	0.06
74.4 ± 4.9	21.0	13.0	0.59	0.10	0.10	0.05
105.1 ± 5.2	37.9	20.5	0.57	0.07	0.07	0.04
131.5 ± 3.2	35.6	16.9	0.39	0.14	0.14	0.05
145.8 ± 0.8	0.2	8.6	0.27	1.27	1.27	1.26
θ = 30° from 0.46-g/cm² H_2O, $(\frac{\delta\sigma}{\sigma})_{na}$ = 4.9%						(Index 11270)
21.6 ± 0.2	4.1	3.5	1.14	0.14	0.12	0.11
25.7 ± 0.4	3.7	3.1	1.15	0.14	0.13	0.11
29.3 ± 0.5	3.3	2.9	1.34	0.13	0.12	0.09
33.3 ± 0.9	4.6	3.1	1.07	0.15	0.14	0.10
38.0 ± 1.5	4.2	3.3	0.88	0.21	0.21	0.13
44.3 ± 2.3	7.3	4.6	1.12	0.16	0.15	0.08
54.2 ± 3.3	11.8	7.1	1.14	0.12	0.11	0.6
70.9 ± 4.7	19.3	11.9	1.17	0.11	0.10	0.05
100.0 ± 5.4	35.0	19.9	1.47	0.08	0.06	0.03
127.9 ± 3.6	37.6	17.9	0.85	0.16	0.15	0.04
141.1 ± 0.9	5.2	11.9	0.49	0.22	0.21	0.14
θ = 30° from 0.57-g/cm² D_2O, $(\frac{\delta\sigma}{\sigma})_{na}$ = 4.0%						(Index 12048)
22.4 ± 0.3	4.5	3.9	1.08	0.13	0.12	0.10
26.9 ± 0.5	3.9	3.4	0.90	0.15	0.14	0.12
31.5 ± 0.8	5.1	3.4	1.08	0.13	0.13	0.09
35.9 ± 1.3	3.5	3.2	1.03	0.19	0.18	0.11
40.8 ± 2.1	5.1	3.9	0.88	0.22	0.21	0.11
48.1 ± 8.9	8.9	5.5	0.91	0.17	0.16	0.08
60.2 ± 4.9	14.2	8.6	1.10	0.15	0.15	0.05
81.3 ± 7.3	24.2	15.2	1.10	0.14	0.13	0.04
113.3 ± 7.4	41.6	20.5	1.28	0.11	0.10	0.03
134.9 ± 3.0	24.3	15.2	1.29	0.29	0.29	0.04

Tables of Measured Cross Sections - cont.

E_k (MeV)	Δ_k (MeV)	$\sqrt{V_k(E)}$ (MeV)	$\sigma(\theta,E_k)$ (mb MeV^{-1} steradian^{-1})	Relative Errors Combined	Assoc	Count
	$\theta = 30^\circ$ from 0.55-g/cm^2 Al, $(\frac{\delta\sigma}{\sigma})_{na}$ = 2.4%					(Index 12014)
20.8 ± 0.1	3.8	3.3	1.3	0.13	0.13	0.12
24.6 ± 0.2	3.4	2.9	1.2	0.14	0.14	0.13
28.6 ± 0.5	4.3	2.9	1.1	0.13	0.13	0.11
33.2 ± 0.8	4.7	2.9	1.3	0.14	0.14	0.10
38.1 ± 1.4	4.4	3.3	1.0	0.21	0.21	0.14
44.5 ± 2.2	7.6	4.7	0.99	0.15	0.15	0.10
54.7 ± 3.1	12.1	7.3	1.16	0.10	0.10	0.07
72.0 ± 4.1	19.9	12.3	1.06	0.08	0.08	0.06
102.0 ± 4.2	36.1	20.4	0.96	0.07	0.07	0.04
129.9 ± 2.5	37.5	18.1	0.56	0.13	0.13	0.06
143.0 ± 0.6	4.8	12.0	0.32	0.25	0.25	0.23
	$\theta = 30^\circ$ from 0.72-g/cm^2 Co, $(\frac{\delta\sigma}{\sigma})_{na}$ = 2.8%					(Index 11246)
21.5 ± 0.2	4.3	3.5	2.2	0.14	0.14	0.13
25.7 ± 0.3	3.7	3.1	2.0	0.16	0.16	0.14
29.4 ± 0.5	3.4	3.0	2.4	0.14	0.14	0.12
33.4 ± 0.9	4.6	3.1	1.9	0.16	0.16	0.13
38.2 ± 1.5	4.3	3.4	1.4	0.24	0.24	0.18
44.5 ± 2.3	7.3	4.6	1.8	0.16	0.16	0.11
54.4 ± 3.4	11.8	7.1	1.6	0.13	0.13	0.09
71.1 ± 4.8	19.3	11.9	1.8	0.11	0.11	0.06
100.4 ± 5.5	35.0	20.1	1.3	0.08	0.08	0.06
129.0 ± 3.6	39.0	18.3	0.83	0.16	0.16	0.07
142.7 ± 0.9	5.7	12.2	0.51	0.29	0.29	0.24
	$\theta = 30^\circ$ from 0.90-g/cm^2 Bi, $(\frac{\delta\sigma}{\sigma})_{na}$ = 2.0%					(Index 12002)
20.1 ± 0.2	3.5	3.0	3.1	0.23	0.23	0.23
23.5 ± 0.2	3.2	2.7	3.7	0.21	0.21	0.21
27.2 ± 0.4	4.0	2.7	3.7	0.18	0.18	0.17
31.4 ± 0.7	4.3	2.8	3.8	0.17	0.17	0.15
35.6 ± 1.1	3.8	2.9	4.4	0.20	0.20	0.15
40.9 ± 1.8	5.7	3.9	2.5	0.26	0.26	0.22
48.8 ± 2.6	9.8	5.8	3.2	0.15	0.15	0.12
62.1 ± 3.6	15.4	9.2	3.0	0.12	0.12	0.09
85.3 ± 4.4	26.7	16.7	2.5	0.10	0.10	0.09
118.4 ± 3.5	44.0	20.9	1.8	0.12	0.12	0.08
138.6 ± 1.1	20.2	15.0	1.2	0.18	0.18	0.14

Tables of Measured Cross Sections - cont.

E_k (MeV)	Δ_k (MeV)	$\sqrt{V_k(E)}$ (MeV)	$\sigma(\theta,E_k)$ (mb MeV^{-1} steradian^{-1})	Relative Errors Combined	Assoc	Count
	$\theta = 45^\circ$ from 0.55-g/cm^2 Aℓ, $(\frac{\delta\sigma}{\sigma})_{na} = 2.3\%$					(Index 12160)
20.4 ± 0.2	4.0	3.4	1.28	0. 0	0.10	0.07
24.8 ± 0.5	4.4	3.1	0.95	0.12γ	0.12	0.09
29.3 ± 0.8	4.3	3.0	0.96	0.13	0.13	0.08
33.6 ± 1.3	4.0	3.1	1.07	0.18	0.18	0.08
39.4 ± 2.5	6.1	4.5	0.97	0.24	0.24	0.07
49.7 ± 4.4	12.7	8.0	0.98	0.17	0.17	0.05
71.4 ± 7.1	25.2	17.1	0.79	0.13	0.13	0.04
107.6 ± 7.0	49.6	24.0	0.39	0.11	0.11	0.04
130.7 ± 2.6	27.0	18.1	0.18	0.22	0.22	0.08
	$\theta = 45^\circ$ from 0.70-g/cm^2 Co, $(\frac{\delta\sigma}{\sigma})_{na} = 3.0\%$					(Index 12138)
20.8 ± 0.2	4.3	3.5	2.15	0.10	0.10	0.07
25.4 ± 0.5	4.6	3.2	1.89	0.12	0.12	0 0.08
30.1 ± 0.9	4.5	3.2	1.85	0.13	0.13	0.08
34.7 ± 1.5	4.2	3.3	0.91	0.19	0.19	0.08
41.3 ± 2.7	7.0	5.1	1.90	0.22	0.22	0.06
52.9 ± 4.9	14.5	9.2	1.63	0.18	0.18	0.05
78.3 ± 7.5	29.4	19.8	1.14	0.12	0.11	0.04
114.6 ± 6.6	52.1	23.7	0.41	0.15	0.15	0.05
134.7 ± 2.2	18.4	17.2	0.13 γ	0.21	0.20	0.13
	$\theta = 60^\circ$ from 0.44-g/cm^2 H_2O, $(\frac{\delta\sigma}{\sigma})_{na} = 5.2\%$					(Index 12244)
21.0 ± 0.2	4.5	3.6	0.84	0.11	0.10	0.08
25.3 ± 0.4	3.7	3.1	1.06	0.11	0.10	0.07
29.5 ± 0.7	4.3	3.1	1.28	0.12	0.11	0.06
33.7 ± 1.2	4.0	3.1	1.59	0.16	0.16	0.06
39.5 ± 2.2	6.1	4.5	1.61	0.23	0.23	0.04
49.8 ± 4.0	12.6	8.0	0.80	0.16	0.15	0.04
71.3 ± 5.9	25.1	16.9	0.34	0.11	0.10	0.05
105.4 ± 5.3	47.2	22.3	0.114	0.14	0.13	0.07
126.2 ± 1.8	22.4	16.5	0.021	0.39	0.38	0.35

Tables of Measured Cross Sections - cont.

E_k (MeV)	Δ_k (MeV)	$\sqrt{V_k(E)}$ (MeV)	$\sigma(\theta,E_k)$ (mb MeV^{-1} steradian^{-1})	Relative Errors Combined	Assoc	Count
	$\theta = 60^\circ$ from 0.55-g/cm^2 Al, $(\frac{\delta\sigma}{\sigma})_{na} = 2.6\%$					(Index 12234)
20.4 ± 0.2	4.0	3.4	0.90	0.11	0.11	0.09
24.8 ± 0.4	4.4	3.1	0.90	0.11	0.11	0.08
29.3 ± 0.8	4.3	3.0	0.73	0.14	0.14	0.09
33.6 ± 1.3	4.0	3.1	0.63	0.19	0.19	0.11
39.4 ± 2.5	6.1	4.5	0.68	0.25	0.25	0.09
49.7 ± 4.4	12.7	8.0	0.63	0.18	0.18	0.06
71.3 ± 7.0	25.2	17.0	0.40	0.13	0.13	0.05
106.7 ± 6.8	48.7	23.3	0.133	0.13	0.13	0.07
128.8 ± 2.5	25.0	17.04	0.039	0.30	0.30	0.22
	$\theta = 60^\circ$ from 0.70-g/cm^2 Co, $(\frac{\delta\sigma}{\sigma})_{na} = 3.0\%$					(Index 12264)
21.0 ± 0.2	4.6	3.5 γ	1.66	0.11	0.11	0.09
25.3 ± 0.3	3.7	3.1	1.56	0.13	0.12	0.10
29.4 ± 0.6	4.2	3.1	1.14	0.15	0.15	0.12
33.6 ± 1.0	3.9	3.2	1.06	0.20	0.19	0.14
39.2 ± 2.0	5.9	4.4	1.21	0.23	0.23	0.10
49.2 ± 3.5	12.2	7.8	1.09	0.14	0.14	0.07
70.0 ± 5.1	24.2	16.5	0.68	0.10	0.09	0.06
106.1 ± 4.5	48.7	24.0	0.19	0.13	0.13	0.09
130.0 ± 1.5	29.6	18.4	0.042	0.34	0.34	0.32
	$\theta = 90^\circ$ from 0.72-g/cm^2 Al, $(\frac{\delta\sigma}{\sigma})_{na} = 2.7\%$					(Index 12176)
22.4 ± 0.2	5.0	4.1	0.57	0.12	0.11	0.10
27.8 ± 0.4	5.3	3.8	0.39	0.14	0.14	0.11
33.4 ± 0.9	5.3	3.7	0.27	0.18	0.18	0.13
39.5 ± 1.9	5.6	4.6	0.22	0.26	0.25	0.15
49.2 ± 3.4	11.7	7.6	0.12	0.19	0.19	0.14
68.9 ± 5.0	23.2	15.7	0.072	0.14	0.14	0.12
102.5 ± 4.3	45.4	22.2	0.13	0.25	0.25	0.23
124.4 ± 1.4	26.2	16.8	0.006	0.43	0.43	0.41

Tables of Measured Cross Sections - cont.

E_k (MeV)	Δ_k (MeV)	$\sqrt{V_k(E)}$ (MeV)	$\sigma(\theta,E_k)$ (mb MeV^{-1} steradian^{-1})	Relative Errors Combined	Assoc	Count
	$\theta = 90^\circ$ from 0.91-g/cm^2 Co, $(\frac{\delta\sigma}{\sigma})_{na} = 2.8\%$					(Index 12200)
23.1 ± 0.2	5.8	4.4	0.79	0.12	0.12	0.10
28.6 ± 0.5	4.5	3.8	0.63	0.15	0.15	0.12
33.7 ± 1.0	5.3	3.8	0.47	0.18	0 0.18	0.13
39.8 ± 2.1	5.6	4.6	0.44	0.25	0.25	0.13
49.5 ± 3.7	11.7	7.6	0.30	0.18	0.18	0.11
69.2 ± 5.8	23.1	15.8	0.13	0.15	0.15	0.11
104.3 ± 6.7	46.9	23.5	0.035	0.18	0.18	0.16
128.3 ± 2.2	30.4	18.1	0.022	0.30	0.30	0.24
	$\theta = 120^\circ$ from 0.72-g/cm^2 Co, $(\frac{\delta\sigma}{\sigma})_{na} = 2.7\%$					(Index 12214)
21.1 ± 0.3	4.6	3.6	0.62	0.16	0.16	0.14
25.5 ± 0.6	3.7	3.2	0.37	0.22	0.22	0.21
29.6 ± 0.9	4.3	3.2	0.30	0.21	0.21	0.18
33.9 ± 1.5	4.0	3.2	0.25	0.27	0.27	0.21
39.6 ± 2.7	6.0	4.6	0.10	0.44	0.44	0.36
49.9 ± 4.9	12.7	8.0	0.09	0.28	0.27	0.19
71.5 ± 8.1	25.1	17.0	0.036	0.27	0.26	0.22
106.2 ± 8.0	47.9	22.8	0.004	0.52	0.52	0.50
127.5 ± 3.0	23.6	16.9	0.018	0.40	0.40	0.32